Draft version August 5, 2015
Preprint typeset using LaTeX style emulateapj v. 5/2/11

OPTICAL AND NEAR-INFRARED OBSERVATIONS OF SN 2013DX ASSOCIATED WITH GRB 130702A

V. L. Toy[1], S. B. Cenko[2,3], J. M. Silverman[4,5], N. R. Butler[6], A. Cucchiara[7], A. M. Watson[8], D. Bersier[9], D. A. Perley[10,11], R. Margutti[12], E. Bellm[10], J. S. Bloom[13], Y. Cao[10], J. I. Capone[1], K. Clubb[13], A. Corsi[14], J. A. de Diego[8], A. V. Filippenko[13], O. D. Fox[13], A. Gal-Yam[15], N. Gehrels[2], L. Georgiev[8], J. J. González[8], M. M. Kasliwal[16], P. L. Kelly[13], S. R. Kulkarni[10], A. S. Kutyrev[2], W. H. Lee[8], J. X. Prochaska[17], E. Ramirez-Ruiz[17], M. G. Richer[8], C. Román[8], L. Singer[18,7], D. Stern[19], E. Troja[2,1], S. Veilleux[1,3]

Draft version August 5, 2015

ABSTRACT

We present optical and near-infrared light curves and optical spectra of SN 2013dx, associated with the nearby (redshift 0.145) gamma-ray burst GRB 130702A. The prompt isotropic gamma-ray energy released from GRB 130702A is measured to be $E_{\gamma,\rm iso} = 6.4^{+1.3}_{-1.0} \times 10^{50}$ erg (1 keV to 10 MeV in the rest frame), placing it intermediate between low-luminosity GRBs like GRB 980425/SN 1998bw and the broader cosmological population. We compare the observed $g'r'i'z'$ light curves of SN 2013dx to a SN 1998bw template, finding that SN 2013dx evolves $\sim 20\%$ faster (steeper rise time), with a comparable peak luminosity. Spectroscopically, SN 2013dx resembles other broad-lined Type Ic supernovae, both associated with (SN 2006aj and SN 1998bw) and lacking (SN 1997ef, SN 2007I, and SN 2010ah) gamma-ray emission, with photospheric velocities around peak of $\sim 21{,}000\,\rm km\,s^{-1}$. We construct a quasi-bolometric ($g'r'i'z'yJH$) light curve for SN 2013dx, and, together with the photospheric velocity, we derive basic explosion parameters using simple analytic models. We infer a ^{56}Ni mass of $M_{\rm Ni} = 0.38 \pm 0.01\,\rm M_\odot$, an ejecta mass of $M_{\rm ej} = 3.0 \pm 0.1\,\rm M_\odot$, and a kinetic energy of $E_{\rm K} = (8.2 \pm 0.40) \times 10^{51}$ erg (statistical uncertainties only), consistent with previous GRB-associated SNe. When considering the ensemble population of GRB-associated SNe, we find no correlation between the mass of synthesized ^{56}Ni and high-energy properties, despite clear predictions from numerical simulations that $M_{\rm Ni}$ should correlate with the degree of asymmetry. On the other hand, $M_{\rm Ni}$ clearly correlates with the kinetic energy of the supernova ejecta across a wide range of core-collapse events.

Subject headings: gamma-ray burst: individual (GRB 130702A) — supernovae: individual (SN 2013dx)

[1] Department of Astronomy, University of Maryland, College Park, MD 20742, USA
[2] NASA, Goddard Space Flight Center, Greenbelt, MD 20771, USA
[3] Joint Space-Science Institute, University of Maryland, College Park, MD 20742, USA
[4] Department of Astronomy, University of Texas at Austin, Austin, TX 78712, USA
[5] NSF Astronomy and Astrophysics Postdoctoral Fellow
[6] School of Earth & Space Exploration, Arizona State University, AZ 85287, USA
[7] NASA Postdoctoral Program Fellow, Goddard Space Flight Center, Greenbelt, MD 20771, USA
[8] Instituto de Astronomía, Universidad Nacional Autońoma de México, Apartado Postal 106, 22800 Ensenada, Baja California, México
[9] Astrophysics Research Institute, Liverpool John Moores University, Liverpool L3 5RF, UK
[10] Department of Astronomy, California Institute of Technology, MC 249-17, 1200 East California Blvd, Pasadena CA 91125, USA
[11] Hubble Fellow
[12] Harvard-Smithsonian Center for Astrophysics, 60 Garden St., Cambridge, MA 02138, USA
[13] Department of Astronomy, University of California, Berkeley, CA 94720-3411
[14] Department of Physics, Texas Tech University, Box 41051, Lubbock, TX 79409-1051
[15] Department of Particle Physics and Astrophysics, Weizmann Institute of Science, Rehovot 7610001, Israel
[16] Observatories of the Carnegie Institution for Science, 813 Santa Barbara Street, Pasadena CA 91101, USA
[17] Department of Astronomy and Astrophysics, UCO/Lick Observatory, University of California, 1156 High Street, Santa Cruz, CA 95064, USA
[18] LIGO Laboratory, California Institute of Technology, Pasadena, CA 91125, USA
[19] Jet Propulsion Laboratory, California Institute of Technology, Pasadena, CA 91109

1. INTRODUCTION

The evidence for the association between long-duration gamma-ray bursts (GRBs) and the death of massive stars has been steadily growing over the last two decades (see Woosley & Bloom 2006 and Hjorth & Bloom 2012 for reviews). The first direct evidence of this link was a spatially and temporally coincident supernova (SN), SN 1998bw, with GRB 980425 at redshift $z = 0.0085$ (Galama et al. 1998; Iwamoto et al. 1998; Kulkarni et al. 1998). Since SN 1998bw, there have been a number of spectroscopically confirmed SNe associated with GRBs: GRB 030329/SN 2003dh (Stanek et al. 2003; Matheson et al. 2003), GRB 031203/SN 2003lw (Malesani et al. 2004; Gal-Yam et al. 2004; Thomsen et al. 2004), GRB 060218/SN 2006aj (Campana et al. 2006; Modjaz et al. 2006a; Mirabal et al. 2006; Ferrero et al. 2006; Sollerman et al. 2006; Pian et al. 2006; Kocevski et al. 2007), GRB 091127/SN 2009nz (Cobb et al. 2010; Berger et al. 2011), GRB 100316D/SN 2010bh (Starling et al. 2011; Bufano et al. 2012; Olivares E. et al. 2012a; Cano et al. 2011a; Chornock et al. 2010), GRB 120422A/SN 2012bx (Melandri et al. 2012; Schulze et al. 2014), GRB 130427A/SN 2013cq (Xu et al. 2013; Levan et al. 2014; Melandri et al. 2014; Perley et al. 2014), and GRB 140606B/iPTF14bfu (Cano et al. 2015).

While most, if not all low-z long-duration GRBs appear to be accompanied by SNe (the exceptions being GRB 060614 and GRB 060505; Fynbo et al. 2006; Gal-Yam et al. 2006; Della Valle et al. 2006), only a small fraction of core-collapse explosions are capable of generating relativistic ejecta (Berger et al. 2003; Soderberg et al. 2010; Bietenholz et al. 2014). Even when limited to the specific subtype of SNe associated with GRBs, the broad-lined Type Ic SNe, those with and without relativistic ejecta appear to be indistinguishable based on their light curves (e.g., Drout et al. 2011). However, spectra of the host galaxies reveal that GRB-SNe prefer more metal-poor environments than Type Ic-BL SNe without associated GRBs (Modjaz et al. 2008; Graham & Fruchter 2013).

Furthermore, within the GRB population, there is a considerable diversity in the observed prompt gamma-ray energies spanning six orders of magnitude from $E_{\gamma,\rm iso} = 10^{48}$–$10^{54}$ erg. It has been suggested that low-luminosity GRBs ($E_{\gamma,\rm iso} \lesssim 10^{49}$ erg) have "failed" jets that cannot pierce their stellar envelope and instead dissipate energy into the star to create relativistic shock breakout (Bromberg et al. 2011; Margutti et al. 2014; Nakar 2015). But despite their very different appearance at high energies, as of yet there is no clear distinction between SNe associated with low-luminosity GRBs (e.g., SN 1998bw) and the larger (observed) cosmological population (e.g., SN 2003dh, SN 2013cq).

With still only a handful of well-observed examples, each new nearby GRB affords a unique opportunity to understand the *central engine* powering these outflows. In particular, we can probe the progenitor from two different angles by studying the SN simultaneously with the GRB. Here we present observations of SN 2013dx associated with GRB 130702A. At $z = 0.145$, SN 2013dx is sufficiently nearby to enable a detailed photometric and spectroscopic study of the SN evolution. Furthermore, with $E_{\gamma,\rm iso} = 6.4 \times 10^{50}$ erg (for 1 keV to 10 MeV in the rest frame), the prompt-emission properties place GRB 130702A between most low-luminosity GRBs and the more energetic cosmological population.

Throughout this paper we use the convention $F_\nu(t) \propto \nu^{-\beta} t^{-\alpha}$ and photon index $\Gamma = \beta+1$. We assume a ΛCDM model with $\rm H_0 = 69.6\ km\ s^{-1}\ Mpc^{-1}$, $\Omega_m = 0.286$, and $\Omega_\Lambda = 0.714$ (Bennett et al. 2014). All photometry is in the AB system (Oke & Gunn 1983), and quoted uncertainties are 1σ (68%) confidence intervals unless otherwise noted. Dates and times are UT in all cases.

2. GRB 130702A/SN 2013DX

GRB 130702A was detected by the Gamma-Ray Burst Monitor (GBM; Meegan et al. 2009) on the *Fermi* satellite at 00:05:23.079 on 2013 July 2 (Collazzi & Connaughton 2013). As observed by the GBM, the prompt-emission duration[20] was $T_{90} \approx 59$ s (50–300 keV). High-energy emission was also detected by the *Fermi* Large Area Telescope (LAT; Atwood et al. 2009; Cheung et al. 2013), as well as by Konus-Wind (Golenetskii et al. 2013). We adopted the Konus-Wind 20–1200 keV fluence of $f_\gamma = (6.7 \pm 0.8) \times 10^{-6}\ \rm erg\ cm^{-2}$ (assuming a power-law spectrum with photon index $\Gamma = 1.87 \pm 0.11$).

Employing the wide-field imaging and rapid transient identification capabilities of the Intermediate Palomar Transient Factory (iPTF; Law et al. 2009; Rau et al. 2009), Singer et al. (2013b) discovered the optical afterglow of GRB 130702A. The source, also referred to as iPTF13bxl, is located at (J2000.0) coordinates $\alpha = 14^{\rm h}29^{\rm m}14^{\rm s}.78$, $\delta = +15^\circ46'26''.4$.

Subsequently, the host-galaxy redshift of GRB 130702A was determined to be $z = 0.145$ based on the detection of narrow emission lines ([O III] and Hα) at the afterglow location (Mulchaey et al. 2013b,a; D'Avanzo et al. 2013). Several other galaxies at or near this redshift located in the field indicate that GRB 130702A occurred in a group or cluster environment, which is highly unusual for a GRB (Kelly et al. 2013; D'Elia et al. 2015). The GRB host galaxy may be a metal-poor satellite of an adjacent massive spiral (SDSSJ142914.57+154619.3), which has an offset of only ~ 19 kpc in projected distance and $< 60\ \rm km\ s^{-1}$ in line-of-sight velocity (Kelly et al. 2013).

At $z = 0.145$, the observed Konus-Wind fluence corresponds to an isotropic energy release of $E_{\gamma,\rm iso} = 6.4^{+1.3}_{-1.0} \times 10^{50}$ erg (1 keV to 10 MeV in the rest frame). This places GRB 130702A securely between the low-luminosity class of events represented by GRB 980425 / SN 1998bw and typical cosmologically distant events with $E_{\gamma,\rm iso} \gtrsim 10^{52}$ erg.

Butler et al. (2013) reported a flattening of the optical afterglow 5.26 d after the burst. A spectrum taken ~ 6 d after the burst showed broad features resembling those of SN 1998bw (Schulze et al. 2013). Cenko et al. (2013) and D'Elia et al. (2013) obtained spectra that confirm the presence of an emerging supernova, dubbed SN 2013dx, and identify similarities with SN 1998bw and SN 2006aj. D'Elia et al. (2015) (hereafter D15) reported GRB 130702A/SN 2013dx light curve, spectras, and SN energetics properties with which we will com-

[20] T_{90} is defined as the time over which a burst emits from 5% of its total measured counts to 95%.

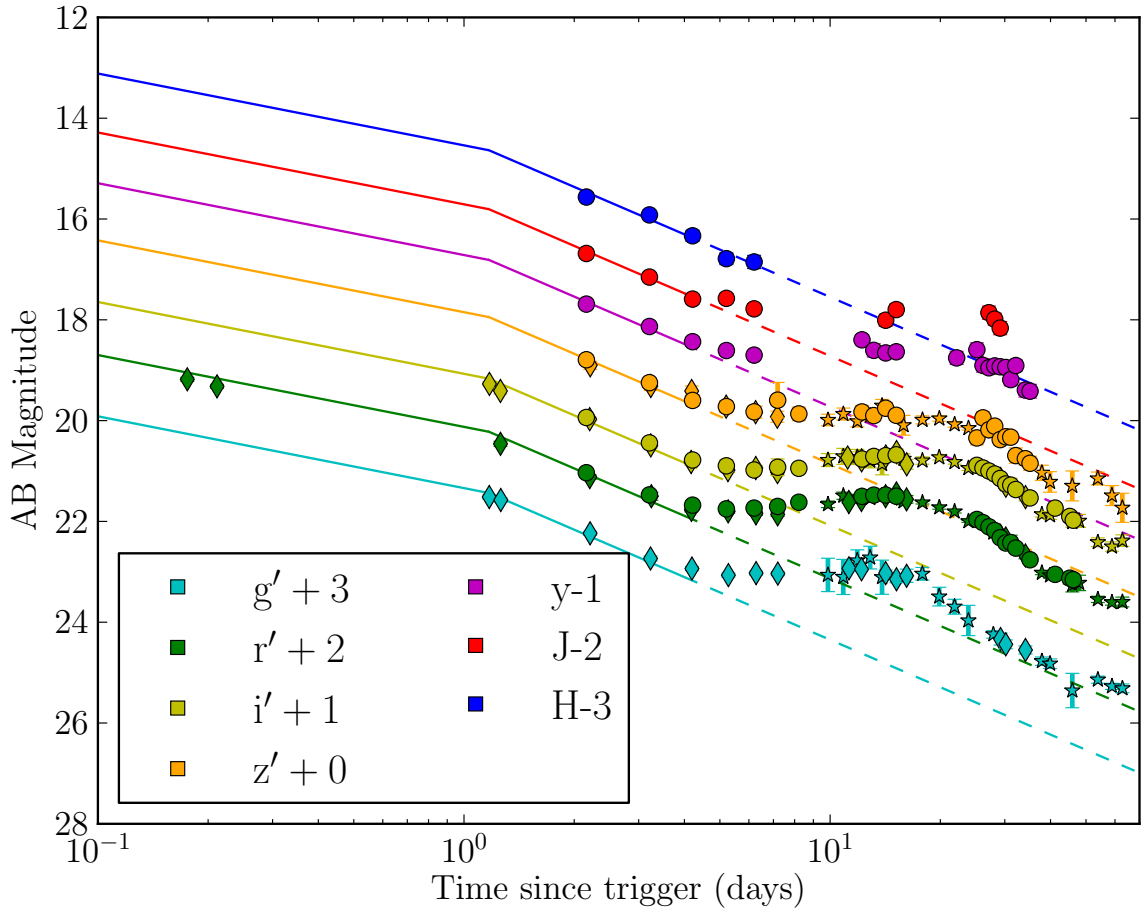

FIG. 1.— Optical and NIR light curves of GRB 130702A, corrected for Galactic extinction and host extinction (assuming $A_{V,\rm host} = 0.10$). Note that the host galaxy contribution is not removed. Diamonds are P48/P60 data, circles are RATIR data, and stars are Liverpool data; errorbars are overplotted on all datapoints. Solid lines indicate power-law fits with $\alpha_1 = 0.57$ and $t_b = 1.17$ d taken from Singer et al. (2013a) and $\alpha_2 = 1.25$ from the XRT power law decay index. Dashed lines mark the extrapolated power law where we assume α_2 for all times beyond t_b.

pare throughout this paper.

3. OBSERVATIONS AND DATA REDUCTION

3.1. *Optical/Near-Infrared Imaging*

We obtained optical and near-infrared (NIR) images of the location of GRB 130702A / SN 2013dx with the robotic Palomar 60 inch telescope (P60; Cenko et al. 2006), the 2 m Liverpool Telescope (LT; Steele et al. 2004), the Reionization and Transients Infrared/Optical camera on the 1.5 m Harold L. Johnson Telescope (RATIR; Butler et al. 2012; Watson et al. 2012), the Large Monolithic Imager on the 4.2 m Discovery Channel Telescope (LMI/DCT), and the Low Resolution Imaging Spectrometer (LRIS; Oke et al. 1995) on the 10 m Keck-I telescope. Additionally, we included early-time Palomar 48-inch r' observations (0.17 d and 0.21 d after the GRB trigger) from Singer et al. (2013a). The reduction procedures for each individual facility are described below, while the resulting photometry is presented in Table 5 and plotted in Figure 1.

3.1.1. *P60 Photometry*

P60 observed the location of GRB 130702A in the g', r', i', and z' filters beginning 1.17 d after the *Fermi* GBM trigger. Basic CCD reductions are provided in real time by a custom IRAF[21]/`PyRAF`[22] pipeline. At later times ($\Delta t \gtrsim 3$ d), images were stacked with `SWarp` (Bertin et al. 2002) on a nightly basis to increase the signal-to-noise ratio (SNR). We performed aperture photometry at the afterglow location, calibrating with respect to nearby point sources from the Sloan Digital Sky Survey (SDSS; Aihara et al. 2011).

3.1.2. *LT Photometry*

LT began observing the location of GRB 130702A with the IO:O CCD camera 9.87 d after the GBM trigger. Observations were obtained in the g', r', i', and z' filters. Standard reduction techniques were applied to detrend the data, and photometry was performed in the same

[21] IRAF is distributed by the National Optical Astronomy Observatory, which is operated by the Association of Universities for Research in Astronomy (AURA) under cooperative agreement with the National Science Foundation (NSF).

[22] See `http://www.stsci.edu/institute/software_hardware/pyraf`.

TABLE 1
Log of Spectroscopic Observations

Δt (d)	Instrument	Exposure (s)	Wavelength Range (nm)	Slit ($''$)	Grating/Grism	Airmass
1.17	DBSP	1800	340–1000	1.0	1200/5000 + 1200/7100	1.06
3.25	DBSP	1800	340–1000	1.0	600/4000 + 316/7500	1.36
6.22	DBSP	1800	340–890	2.0	600/4000 + 600/10000	1.25
9.33	DEIMOS	600	450–950	1.0	600/7500	1.19
11.34	DEIMOS	600	490–1010	1.0	600/7500	1.32
14.21	DBSP	1200	350–1000	1.5	600/4000 + 316/7500	1.27
31.28	DEIMOS	900	450–950	1.0	600/7500	1.30
33.27	LRIS	1200	330–1020	1.0	400/3400 + 400/8500	1.30
330.39	LRIS	1460	330–1020	1.0	400/3400 + 400/8500	1.04

manner as the P60 images (including the same SDSS reference stars for photometric calibration).

3.1.3. *RATIR Photometry*

RATIR obtained simultaneous multi-color ($r'i'z'yJH$) imaging of the location of GRB 130702A beginning 2.16 d after the GBM trigger. The RATIR data were reduced using an automatic `python` pipeline with bias subtraction and twilight flat fielding. Given the lack of a cold shutter in RATIR's design, IR dark frames were not available. Laboratory testing, however, confirmed that the dark current is negligible in both IR detectors (Fox et al. 2012). Astrometric solutions were calculated from `astrometry.net` (Lang et al. 2010) and the individual frames are stacked using `SWarp`.

We performed aperture photometry on the resulting stacked images using `Sextractor` (Bertin & Arnouts 1996) with an inclusion radius determined from the median full width at half-maximum intensity (FWHM) of the images. The resulting instrumental magnitudes were compared to SDSS in the optical and 2MASS (Skrutskie et al. 2006) in the NIR to calculate zeropoints. For the y band, we created a spectral energy distribution (SED) from the combination of optical and NIR catalog sources and interpolated to the appropriate wavelength. To place all photometry on the AB system, we used the J- and H-band offsets from Blanton & Roweis (2007).

3.1.4. *Keck/LRIS Photometry*

The location of GRB 130702A was observed with Keck/LRIS on 2014 May 28 ($\Delta t = 330$ d) in the u', g', and R-band filters. The resulting images were reduced using the `LPipe` package[23]. Because the host galaxy was clearly resolved in some of the better-seeing images (FWHM = $0\farcs75$), we adopted an aperture radius of $1\farcs5$ to incorporate all the flux from the visible extent of the galaxy (Figure 2). Photometric calibration was performed relative to point sources from SDSS.

3.1.5. *Keck/MOSFIRE Photometry*

We imaged the location of GRB 130702A with the Multi-Object Spectrometer For InfraRed Exploration (MOSFIRE; McLean et al. 2012) on the 10 m Keck I telescope on the night of 2014 June 16. Images were obtained in the J and K_s filters and reduced using custom IDL scripts. We performed aperture photometry using a $1\farcs5$ inclusion radius (see § 3.1.4), with photometric calibration relative to 2MASS.

[23] See `http://www.astro.caltech.edu/~dperley/programs/lpipe.html` for details.

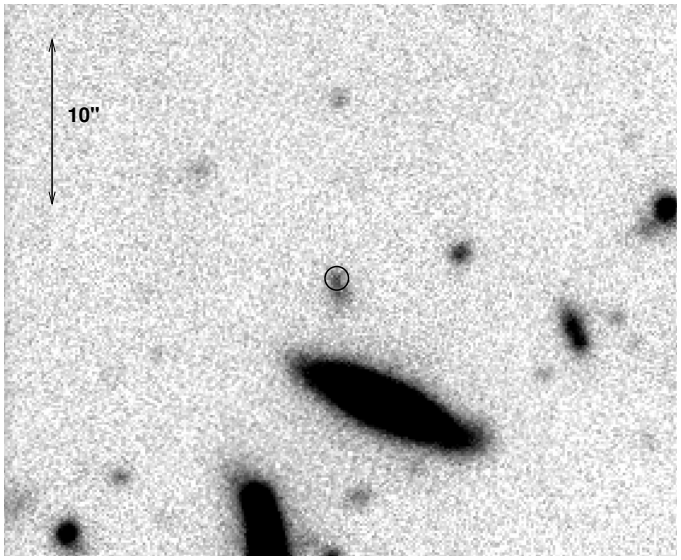

Fig. 2.— Keck/LRIS g'-band image of the host galaxy of GRB 130702A, obtained at $\Delta t = 330.48$ d after the GBM trigger (i.e., when the afterglow and SN emission had faded away). The location of the transient is indicated by the black circle ($0\farcs5$ radius, significantly larger than the actual astrometric uncertainty). The dwarf host is clearly elongated in the N-S direction, with the bulk of the star formation (as evidenced by the transient location and the nebular emission lines) apparent in the northern component. The image is oriented with N up and E to the left.

3.1.6. *LMI/DCT Photometry*

The location of GRB 130702A was observed with LMI/DCT on 2015 March 27 ($\Delta t = 633$ d) in the g', r', i', and z' filters. The resulting images were detrended with a custom IRAF pipeline. Individual frames were astrometrically aligned with `Scamp` (Bertin 2006) and coadded using `SWarp`. Photometry was calculated in the manner described in § 3.1.3.

3.2. *Optical Spectroscopy*

We obtained a series of optical spectra of GRB 130702A, beginning at $\Delta t = 1.17$ d after the *Fermi*-GBM trigger, with the Double Spectrograph (DBSP; Oke & Gunn 1982) on the 5 m Palomar Hale telescope, Keck/LRIS on Keck-I, and the DEep Imaging Multi-Object Spectrograph (DEIMOS; Faber et al. 2003) on the 10 m Keck-II telescope. An observing log is presented in Table 1. All spectra were obtained with the slit oriented at the parallactic angle to minimize differential losses due to atmospheric dispersion (Filippenko 1982; though note also that LRIS employs an Atmospheric Dispersion Corrector to further mitigate

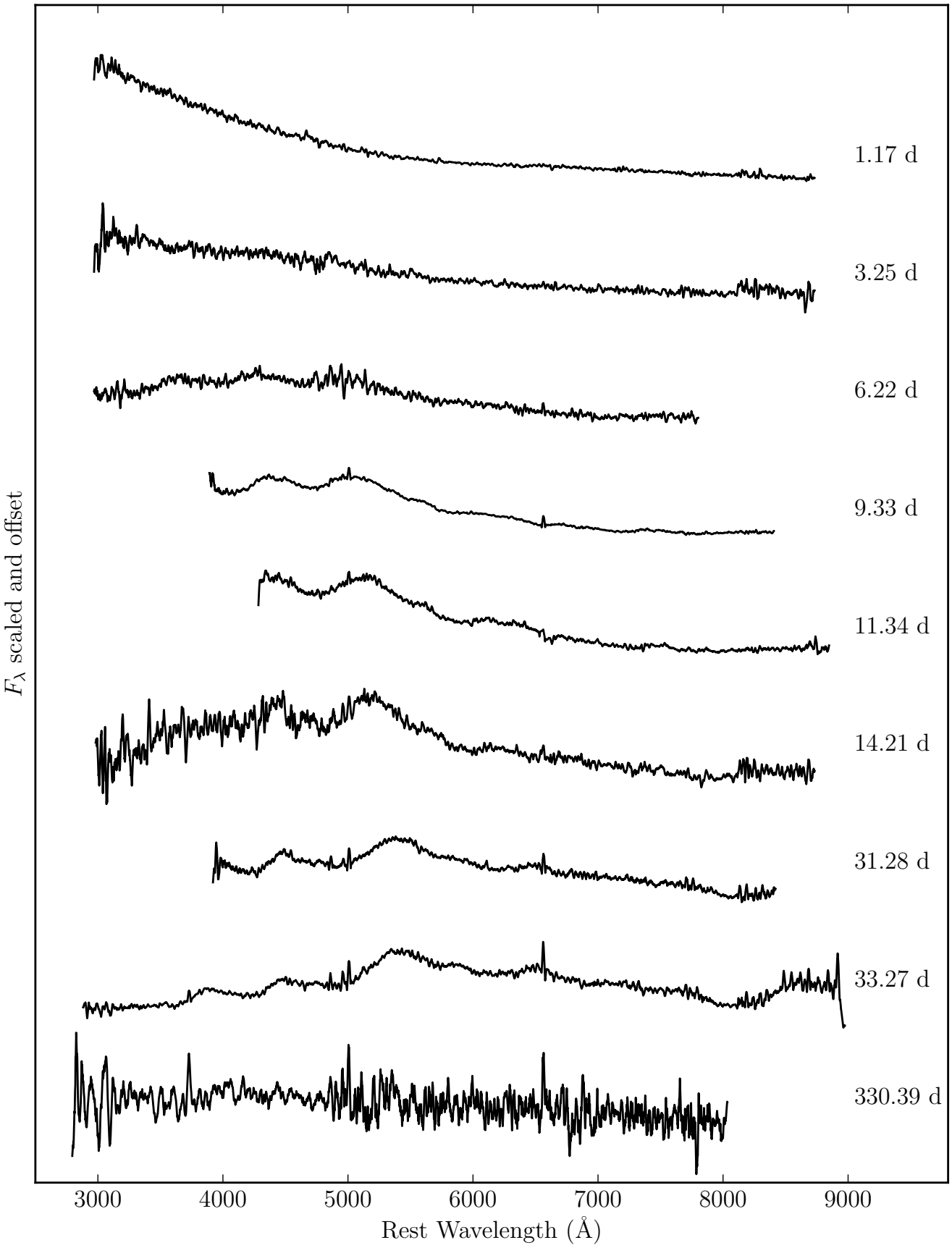

FIG. 3.— Spectra uncorrected for slit losses, extinction, afterglow, or host-galaxy contamination. They are smoothed using a Savitzky-Golay filter with a 30 Å window. Early-time spectra are dominated by the afterglow component. The broad features associated with SN 2013dx become visible after about a week.

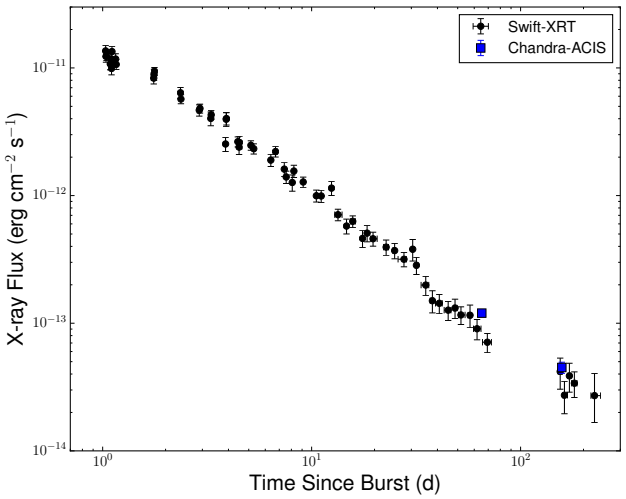

FIG. 4.— X-ray light curve of GRB 130702A.

against differential slit losses). The resulting reduced one-dimensional spectra are displayed in Figure 3.

All spectra were reduced using standard routines and optimally extracted (Horne 1986) within the IRAF environment (see, e.g., Cenko et al. 2008 for details). A dispersion solution was computed using calibration spectra of comparison lamps, and then adjusted for each individual exposure using night-sky emission lines. For the LRIS and DEIMOS spectra, sky background emission was subtracted using the algorithm described by Kelson (2003). Telluric atmospheric absorption features were removed using the continuum from spectrophotometric standard stars (Wade & Horne 1988; Matheson et al. 2000). Finally, a sensitivity function was applied using observations of spectrophotometric standards at a comparable airmass. We caution that the final Keck/LRIS spectrum obtained at $\Delta t = 330.39$ suffered from a failure of the blue shutter, which may impact the relative flux calibration.

Upon publication of this manuscript, all one-dimensional spectra will be made publicly available via the Weizmann Interactive Supernova data REPository (WISeREP; Yaron & Gal-Yam 2012).

3.3. *X-Ray Observations*

The afterglow of GRB 130702A was observed by the X-Ray Telescope (XRT; Burrows et al. 2005) onboard the *Swift* satellite (Gehrels et al. 2004) beginning at $\Delta t = 1.03$ d after the *Fermi*-GBM trigger (e.g., Singer et al. 2013a). We downloaded the X-ray light curves from the XRT Light Curve Repository [24]. The time-averaged spectrum was well described (W-stat = 299.10 for 374 degrees of freedom) by a power-law model, $\Gamma = 1.84 \pm 0.12$, with no evidence for $N_{\rm H}$ in excess of the Galactic value ($N_{\rm H,Gal} = 1.83 \times 10^{20}$ cm^{-2}; Kalberla et al. 2005).

We initiated deep X-ray follow-up observations of GRB 130702A with the *Chandra* X-ray Observatory on 2013 September 5, corresponding to $\Delta t = 65.2$ d since trigger (PI Margutti). The data were reduced with the CIAO software package (version 4.6) and corresponding calibration files. Standard ACIS data filtering has been applied. In 14.9 ks of observations we find clear evidence for X-ray emission at the location of GRB 130702A, with significance $> 50\sigma$. The spectrum was well modeled by an absorbed power law with $\Gamma = 1.66 \pm 0.15$, consistent with the *Swift*-XRT time-averaged spectrum. We found no evidence for an intrinsic absorption component, with a 3σ limit of $N_{\rm H,host} < 1.5 \times 10^{21}$ cm^{-2}. Adopting these spectral parameters, the unabsorbed flux is $F_X = (1.20 \pm 0.08) \times 10^{-13}$ erg s^{-1}cm^{-2} (0.3–10 keV).

A second epoch of *Chandra* observations was obtained on 2013 December 6 ($\Delta t = 157.5$ d) with an exposure time of 34.6 ks. GRB 130702A was clearly detected with significance $> 40\sigma$, which allows us to constrain the spectral evolution (or lack thereof) of GRB 130702A at very late times. Our spectral analysis reveals no evidence for spectral evolution. The best fitting power-law index was $\Gamma = 1.85 \pm 0.16$, with $N_{\rm H,host} < 1.6 \times 10^{21}$ cm^{-2} at 3σ confidence level. The corresponding unabsorbed flux is $F_X = (4.5 \pm 0.45) \times 10^{-14}$ erg s^{-1}cm^{-2} (0.3–10 keV).

The X-ray light curve of GRB 130702A, comprising *Swift*-XRT and *Chandra* observations, is presented in Figure 4.

4. LIGHT-CURVE ANALYSIS

4.1. *Isolating the SN Component*

Emission from the location of GRB 130702A results from three distinct components: the GRB afterglow, the associated SN, and the underlying host galaxy. Here we try to isolate the emission resulting from the associated SN, including a proper accounting for line-of-sight extinction, in order to study the properties of SN 2013dx.

First, we correct our broadband photometry for extinction, both in the Milky Way and in the host galaxy. For the Galactic component, we employ the dust-map calibration of Schlafly & Finkbeiner (2011), resulting in $E(B-V)_{\rm MW} = 0.038$ mag, and the Milky Way extinction law of Cardelli et al. (1989). In order to estimate the host extinction, $A_{V,\rm host}$, we create an SED at $\Delta t = 2.25$ d from linear interpolation. We assume the observed emission at this stage will be dominated by the (synchrotron) afterglow, and thus we fit the SED to a simple power-law model of the form $f_\nu \propto \nu^{-\beta}$ (e.g., Sari et al. 1998). We incorporate $A_{V,\rm host}$ as a free parameter, assuming a Small Magellanic Cloud (SMC)-like extinction law (Pei 1992). We find $A_V = 0.13 \pm 0.23$ mag and $\beta = 0.52 \pm 0.19$ with a reduced $\chi^2_{\rm red} = 0.83$. Adopting Large Magellanic Cloud (LMC) and Milky Way (MW) dust extinction laws did not alter the derived parameters or fit quality. For the rest of this paper we assume $A_{V,\rm host} = 0.10$ mag. This is consistent with other GRB host-extinction values: 50% of GRBs have $A_{V,\rm host} < 0.4$ mag and 87% of GRBs have $A_{V,\rm host} < 2$ mag (Covino et al. 2013).

Next, we attempt to remove any contribution from the afterglow. Singer et al. (2013a) modeled the early-time optical emission ($\Delta t \lesssim 4$ d) as a broken power law with an initial decay index of $\alpha_1 = 0.57 \pm 0.03$ up to the break time, $t_{\rm b} = 1.17 \pm 0.9$ d, after which the model followed a power-law decay index of $\alpha_2 = 1.05 \pm 0.03$. We repeat this analysis with our larger photometric dataset and find largely consistent results. However, even as early as several days post-trigger, the observed emission will likely have some contribution from the emerging SN (e.g., the

[24] See `http://www.swift.ac.uk/xrt_curves` and the associated description in Evans et al. (2009).

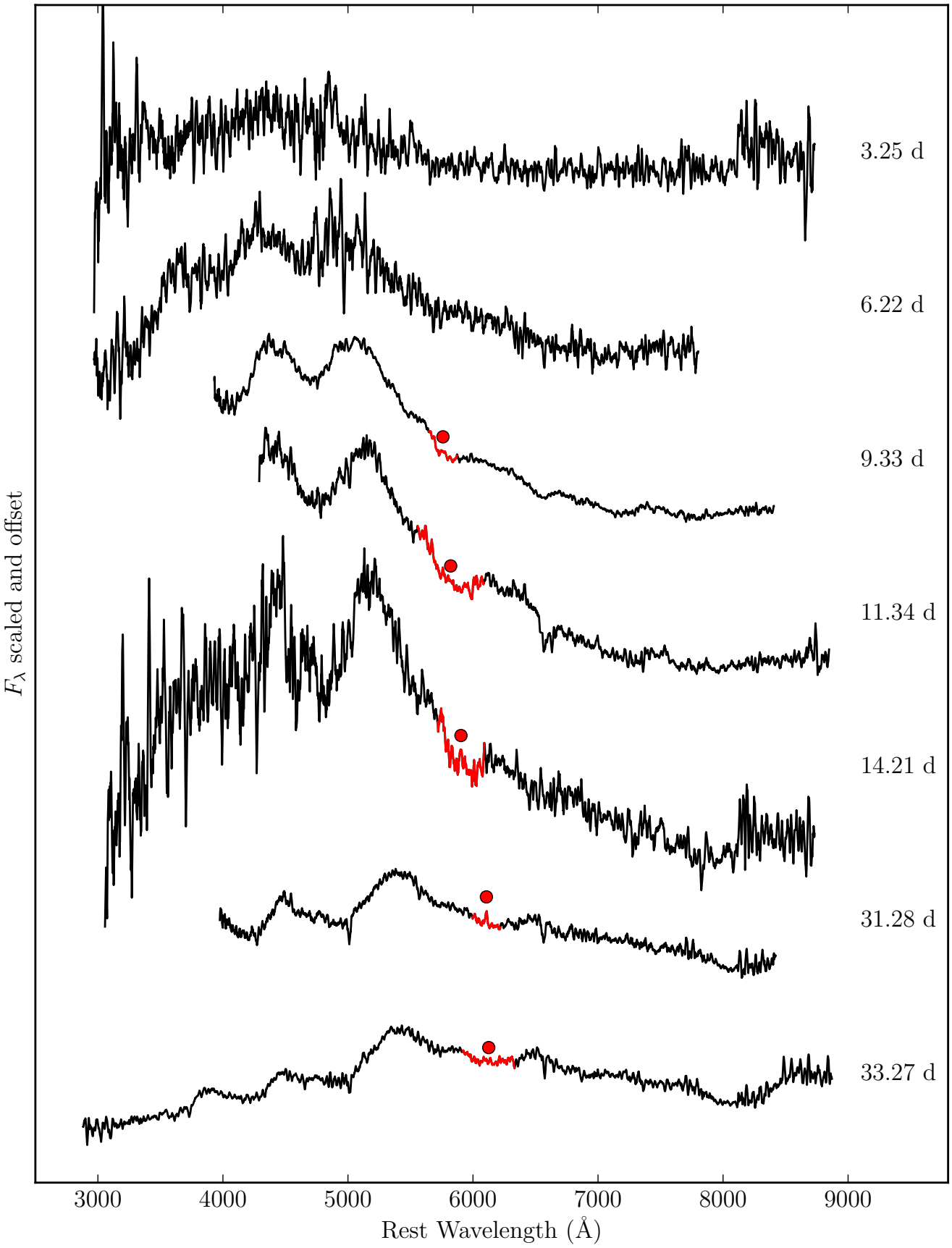

FIG. 5.— SN 2013dx spectra with host galaxy and GRB afterglow removed. They are smoothed using a Savitzky-Golay filter with a 30 Å window. We excluded the spectrum at $t = 1.17$ d because it is dominated by the afterglow. Red filled circles mark the position of Si II λ6355 calculated in § 5.3, used to determine the photospheric velocity of the ejecta. We have highlighted the Si II λ6355 absorption feature in red.

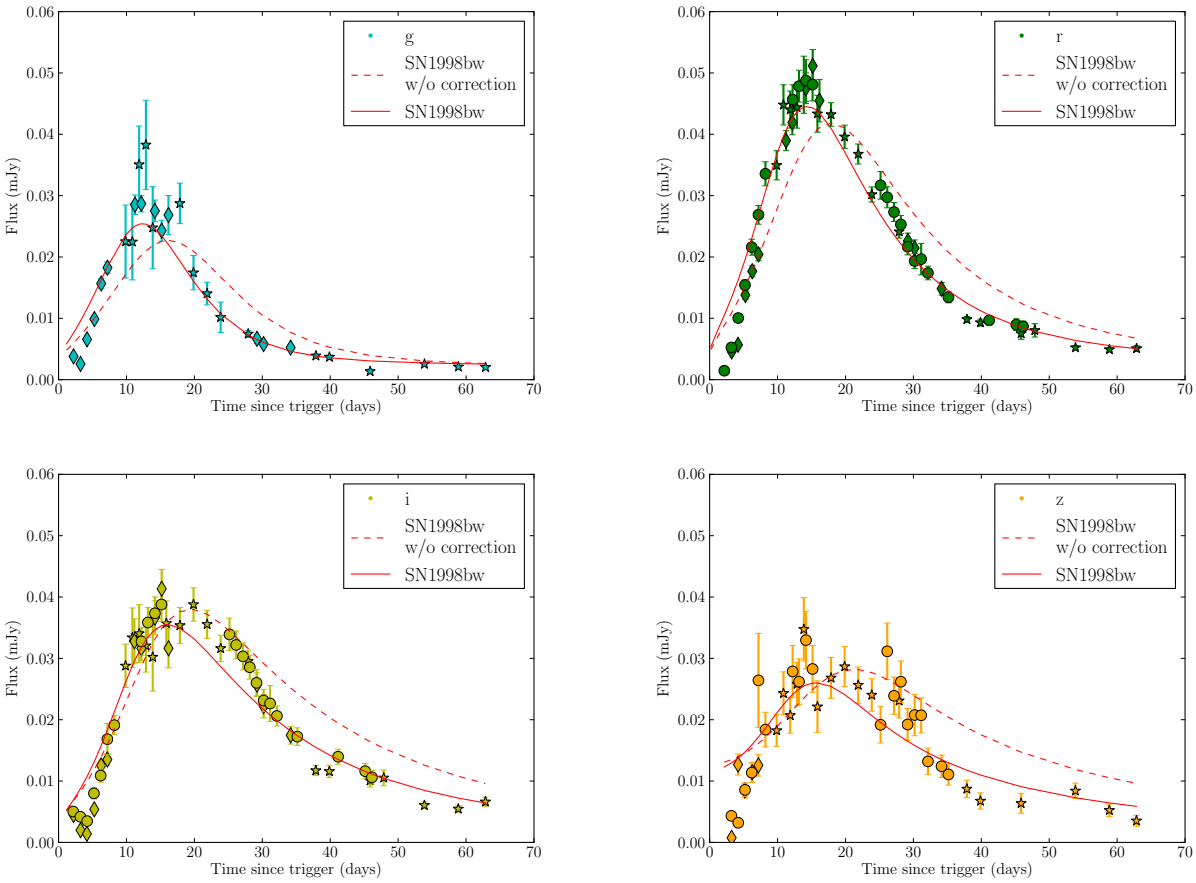

FIG. 6.— Observed SN 2013dx $g'r'i'z'$ data (top left, top right, bottom left, and bottom right, respectively), with synthetic SN 1998bw light-curve fit (dashed red line) and an optimized synthetic SN 1998bw light-curve fit scaled by a peak-amplitude factor k and time-stretch factor s (solid red line; see §4.2) overlaid. SN 1998bw template created from Clocchiatti et al. (2011), Galama et al. (1998), Sollerman et al. (2002), and Patat et al. (2001). Diamonds are P48/P60 data, circles are RATIR data, and stars are Liverpool data.

broad features becoming apparent in the $\Delta t = 3.25$ d DBSP spectrum in Figure 5). Consequently, the true afterglow decay index may be steeper than indicated here.

Instead, we consider the decay of the corresponding X-ray emission, which is unlikely to be contaminated by the SN at $\Delta t \gtrsim 1$ d. We fit the X-ray light curve to a power-law model and find $\alpha_X = 1.25 \pm 0.03$. Combining this with the measured X-ray spectral index from the *Swift*-XRT data, $\beta_X = 0.84 \pm 0.12$, we can use standard afterglow closure relations (e.g., Racusin et al. 2009, and references therein) to evaluate where the X-rays fall on the broadband synchrotron spectrum. The best fit is found for a constant-density circumburst medium with the X-rays falling below the synchrotron cooling frequency, ν_c.

As a result, the optical bandpass must fall below ν_c as well, which is consistent with the measured X-ray to optical spectral index of $\beta_{OX} \approx 0.7$ at $\Delta t = 2$ d. Thus, since the optical emission falls on the same segment of the SED as the X-rays, it should decay with the same power-law index, $\alpha_O = 1.25$. We further assume that both the optical afterglow spectral and temporal indices remain constant in time over the course of our observations. We use this model to calculate the afterglow contribution for all our photometric observations.

We note that this is a significantly shallower decay index than the $\alpha_O = 2.2$ adopted by D15, who did not incorporate multi-wavelength observations into their afterglow analysis. A steeper α_O may overestimate the SN flux at early times, but is negligible at the peak and late times when the SN is significantly brighter than the afterglow.

Finally, we must remove the contribution from the underlying host galaxy. In our best seeing images at late times (FWHM $\approx 0\farcs75$), the host is clearly resolved, with the afterglow/SN location falling on a blue "knot" to the North (Figure 2). This location is also responsible for the nebular emission lines seen in the final Keck/LRIS spectrum (Figure 3).

To remove the host contribution from our photometry, we adopt host flux values from our late-time DCT ($g'r'i'z'$) and Keck/MOSFIRE (J) imaging and directly subtract these from the measured transient fluxes. While this does not account for the resolved nature of the host, since the typical seeing in our SN data ($\approx 1\farcs5$) is comparable to the size of the extended emission, this should have minimal impact on the resulting photometry. We do not have host-galaxy detections in the y and H bands, but the host contribution is negligible compared to the afterglow and SN components.

The resulting SN light curves are displayed in Figure 6. The peak times of the light curves are useful for constraining theoretical models, in particular the convolution of total ejected mass, kinetic energy, and opacity of the SN explosion (via the diffusion time). We

TABLE 2
SN 1998BW TEMPLATE FITS

Filter	s	k	$\chi^2_{\rm red}$
g'	0.78 ± 0.03	1.12 ± 0.04	3.59
r'	0.80 ± 0.01	1.07 ± 0.02	3.85
i'	0.83 ± 0.03	0.93 ± 0.03	3.64
z'	0.74 ± 0.03	0.92 ± 0.05	2.64

measure the rest-frame peak times by fitting a second-order polynomial at $7 \leq \Delta t < 20$ d and find the following: $t_{\rm p}(g') = 11.7 \pm 0.3$ d, $t_{\rm p}(r') = 13.2 \pm 0.3$ d, $t_{\rm p}(i') = 14.7 \pm 0.6$ d, and $t_{\rm p}(z') = 15.1 \pm 1.6$ d (statistical uncertainties only). These values generally agree well with those reported by D15. We do not include peak times for yJH because the data are not well sampled close to the peak.

There is marginal evidence in the i'-band light curve (Figure 6) of a decline in flux at early times ($\Delta t \lesssim 3$ d). This is consistent with early signatures of shock cooling (e.g., SN 2006aj, Campana et al. 2006; SN 2010bh, Cano et al. 2011b). However, shock breakout should be significantly stronger in bluer bands and we see no indication of it in either the g' or r' bands. The relatively bright optical afterglow of GRB 130702A, compared to the optical afterglows of (for example) GRB 060218 and GRB 100316D, greatly complicates isolating the SN component at early times. Thus, it is difficult to reach firm conclusions regarding the presence or absence of a shock-breakout signature.

4.2. *Comparison with SN 1998bw*

Following past studies of GRB-associated SNe in the literature, we next attempt to compare SN 2013dx to the well-studied SN 1998bw (associated with GRB 980425). We create K-corrected synthetic SN 1998bw light curves in the $g'r'i'z'$ filters at the redshift of SN 2013dx, $z = 0.145$, using methods described by Hogg et al. (2002). We utilize SN 1998bw photometry and spectra from Clocchiatti et al. (2011), Galama et al. (1998), Sollerman et al. (2002), and Patat et al. (2001). The K-corrected synthetic SN 1998bw light curves were also time dilated to match the observer frame of SN 2013dx.

Owing to gaps in the temporal coverage of SN 1998bw photometry, especially in the rising phase, we fit the synthetic SN 1998bw light curve in each filter with the empirical functional form from Cano et al. (2011b):

$$U(t) = A + pt\left(\frac{e^{(-t^{\alpha_1}/F)}}{1+e^{(p-t/R)}}\right) + t^{\alpha_2}\log(t^{-\alpha_3}), \quad (1)$$

allowing $A, p, F, R, p, \alpha_1, \alpha_2,$ and α_3 to vary. The resulting SN 1998bw synthetic light curves are plotted as dashed lines in Figure 6.

We then assume the light curves of SN 2013dx in each of our four filters can be modeled by simply varying the peak amplitude (k) and stretch factor (s):

$$L_{rm13dx}(t) = k\, U_{\rm 98bw}(t/s) \quad (2)$$

The resulting fits are plotted in Figure 6, while the measured stretch and amplitude values are displayed in Table 2. We find that SN 2013dx has a peak flux comparable to that of SN 1998bw in all four filters reported here (slightly more luminous in the bluer filters, and slightly less luminous in the redder filters). With a constant stretch value of $s \approx 0.8$ in all four filters, the evolution of SN 2013dx (in particular the rise time) is noticeably faster than that of SN 1998bw.

However, it is also clear from the fits that SN 1998bw is not an ideal match to SN 2013dx, especially in the redder i- and z-band filters. Given these important differences, we refrain from drawing any physical inferences (e.g., $M_{\rm Ni}$, $E_{\rm K}$) from these fits, and instead use the more model-independent bolometric light curve in § 6.

Cano (2014) and Lyman et al. (2014a) suggested that GRB-SNe can be used as standardizable candles. Cano (2014) proposed that s and k (measured relative to SN 1998bw) are analogous to the absolute peak SN magnitude and the amount the light curve fades from maximum light to 15 d later (Δm_{15}) used in the Phillips relation (Phillips 1993) for SNe Ia. We add the uncertainties from our s and k fit in quadrature and find that our measurements of SN 2013dx deviate by 3.7σ from the Cano (2014) fits. The worst fits to Cano (2014) are for g' and r' at 3.7σ; however, z' is within 0.9σ. This further supports the notion that SN 1998bw is not a perfect match for all GRB-associated SNe.

4.3. *Bolometric Light Curve*

We construct the quasi-bolometric light curve of SN 2013dx using our photometry in the g', r', i', z', y, and J filters (H had only upper limits at $\Delta t \gtrsim 5$ d). We include synthetic photometry for $\Delta t = 31.28$ and 33.27 d from our spectra (see § 5.1) to supplement photometric coverage at these epochs. We assume a 10% flux error on all synthetic photometry data points. We convert the extinction, host-galaxy, and afterglow-corrected magnitudes to monochromatic fluxes and create SEDs from linear interpolation of the data for each epoch between 1 to 70 d with 0.25 d spacing. Epochs that are > 0.5 d from observations are removed to mitigate linear interpolation errors, which only affects observations in the y and J bands (see below). We assume that the flux is constant across the bandwidth of each filter and use trapezoidal integration to calculate the quasi-bolometric luminosity. We note that our photometry provides coverage over the observer-frame bandpass 0.4–1.35 μm (rest-frame 0.35–1.18 μm).

At $\Delta t \approx$ 15–25 d and $\Delta t > 35$ d, the y- and J-band data are relatively sparse. We therefore calculate the bolometric luminosity for the entire light curve both including y and J ($g'r'i'z'yJ$) and excluding them ($g'r'i'z'$) to determine the NIR to integrated flux ratio. We find that the fraction of flux at these wavelengths increases monotonically as a function of time, from 13% at $\Delta t \approx 6$ d to 23% at $\Delta t \approx 29$ d. For epochs when only $g'r'i'z'$ observations were available, we add a fractional NIR contribution for the y- and J-band from our linear fit. At late times we adopt the last NIR ratio measurement at $\Delta t \approx 29$ d of $\sim 23\%$ instead of extrapolating our linear fit. This may underestimate the NIR contribution at late times. Our NIR contribution measurements are consistent with an analogous measurement for SN 2008D (Modjaz et al. 2009), though slightly smaller than for SN 2009bb and SN 2010bh (Cano et al. 2011b), which have maximum NIR contributions of 35–45% at $\Delta t \approx 25$ d.

The resulting bolometric light curve is displayed in Figure 7. Our associated uncertainty measurements in-

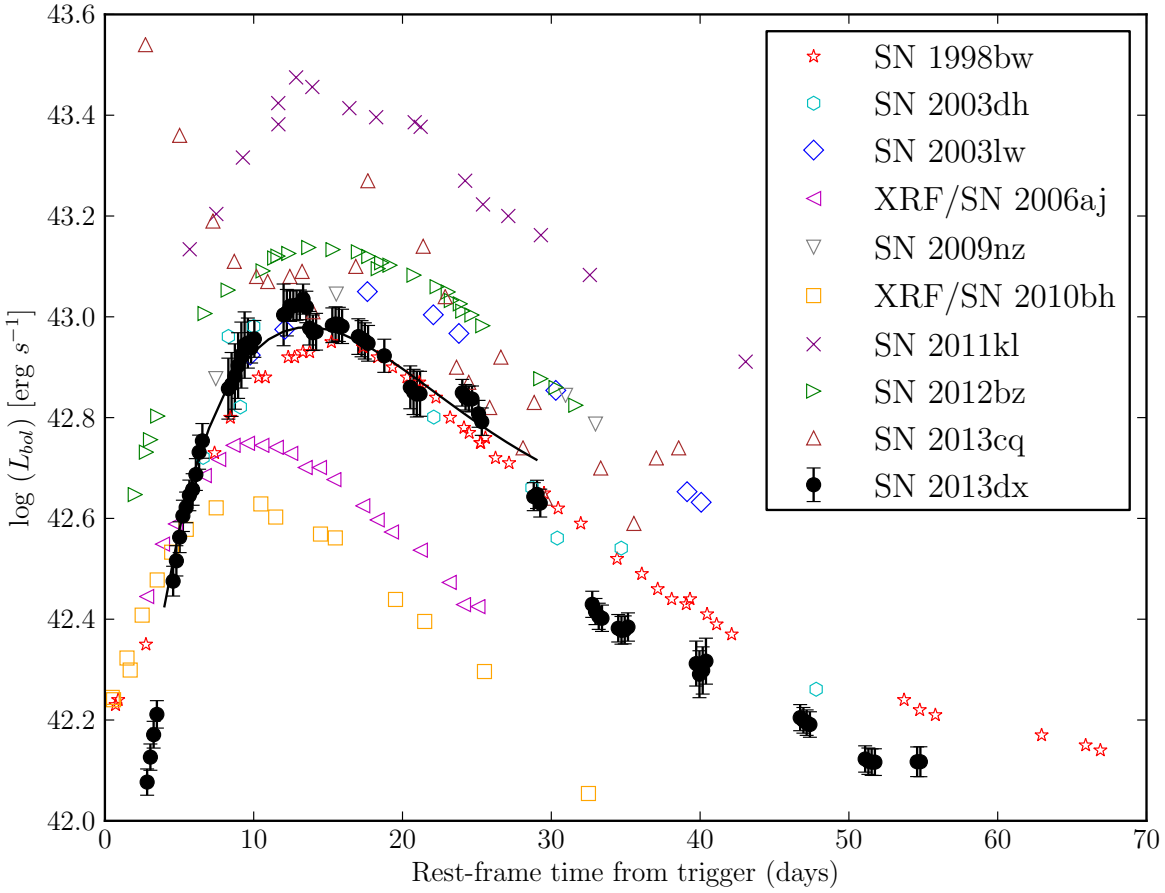

FIG. 7.— $g'r'i'z'yJ$ bolometric light curve fit with Arnett-Valenti relation fit for $4 \leq t \leq 30$ d (solid black line). Bolometric light curves of other spectroscopically confirmed GRB-SNe are included for comparison. Note that these "bolometric" light curves cover different wavelength ranges.

corporate errors from the flux measurements, as well as bandpass uncertainties, but do not include errors introduced from linear interpolation.

Lyman et al. (2014c) have created a model for core-collapse SN bolometric corrections using two filters for nearby events. The corrections include ultraviolet and NIR contributions. Since SN 2013dx is at $z = 0.145$, we use our K-corrected spectra (see §5.1) to extract g' and r' synthetic photometry. We apply the methodology described by Lyman et al. (2014c) and find that this model leads to excellent agreement with our brute-force $g'r'i'z'yJ$ bolometric light curve. This confirms that we are not underestimating the ultraviolet and NIR contributions in our quasi-bolometric light curve.

5. SPECTRAL ANALYSIS

5.1. *Isolating the SN Component*

In a similar manner to that of § 4.1, we wish to isolate the SN component from our spectroscopic observations of GRB 130702A. First, for absolute-flux calibration, we normalize our spectra to (uncorrected) broadband photometry at the appropriate epoch. This accounts for slit losses caused by variable seeing.

We next deredden our spectra of SN 2013dx in an analogous manner to that of § 4.1. This includes contributions from both the Milky Way [$E(B-V) = 0.038$ mag] and the host galaxy ($A_{V,\rm host} = 0.1$ mag).

To remove the afterglow contribution, we assume that the spectrum can be described at all times (and frequencies) as a power law of the form $f_\nu(t,\alpha) \propto t^{-\alpha}\nu^{-\beta}$, with $\alpha = 1.25$ and $\beta = 0.52$ (§ 4.1). We normalize this function to our (extinction-corrected) broadband photometry, and subtract the appropriate power-law model at the epoch of each spectrum.

Finally, we fit the LMI/DCT late-time photometry to a variety of template galaxies from Kinney et al. (1996). Similar to D15, we find that the best-fit template is a starburst galaxy, and we adopted this (appropriately normalized) as the host contribution to the spectra. We take this approach instead of using our final Keck/LRIS spectrum due to the blue shutter failure.

After these corrections, only the SN component remains. Figure 5 displays the resulting spectra of SN 2013dx after smoothing. We exclude the first spectrum ($\Delta t = 1.17$ d) because it is completely afterglow dominated. In addition, we manually excise nebular emission lines from the host galaxy of SN 2013dx.

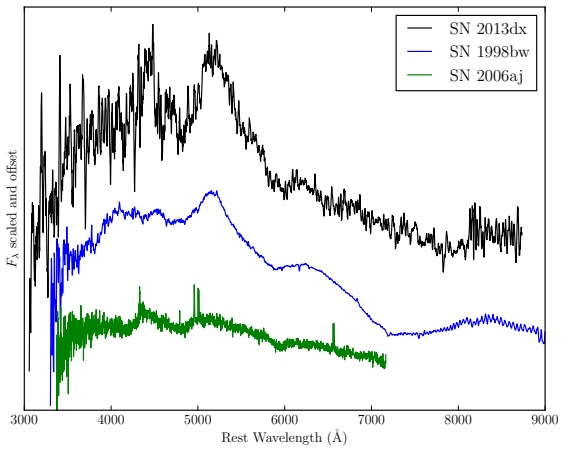

FIG. 8.— Comparison of GRB-SN spectra near maximum light. SN 2013dx spectrum (black) taken at $t = 14.2$ d, closest to maximum light in r' ($\Delta t = 13.2$ d) and i' ($\Delta t = 14.7$ d), smoothed using a Savitzky-Golay filter with 30 Å windows. We overplot SN 1998bw (blue; Patat et al. 2001) at -1 d from maximum light and SN 2006aj (green; Modjaz et al. 2006b) at maximum light for comparison.

TABLE 3
VELOCITY OF SI II λ6355

$t_{\rm obs}$ (days)	Velocity ($\rm km\,s^{-1}$)
9.3	28,100 ± 1000
11.3	25,200 ± 500
14.2	21,300 ± 500
31.3	11,700 ± 500
33.3	10,800 ± 500

5.2. *Comparison with Other Type Ic-BL SNe*

The early-time spectra of SN 2013dx are fairly featureless, but after a week, broad ($v \approx 3 \times 10^4\,\rm km\,s^{-1}$) features appear. Together with the lack of obvious H and He emission, this leads us to classify SN 2013dx as a broad-lined Type Ic SN (Ic-BL), as has been the case for essentially all well-studied GRB-associated SNe thus far (e.g., Woosley & Bloom 2006).

In Figure 8, we plot the spectrum of SN 2013dx obtained around maximum light, along with analogous spectra from the prototypical SN 1998bw (Patat et al. 2001) and SN 2006aj (Modjaz et al. 2006b). All three GRB-SNe show blueshifted, broad-lined Si II λ6355 and a blended Fe II absorption feature around a blueshifted wavelength of 4800 Å. The overall continuum shape of SN 2013dx appears to match that of SN 1998bw more closely than SN 2006aj; however, it appears to have weaker Ca II features than those seen in SN 1998bw.

To search for other similar objects in the literature, we use the cross-correlation tool SN Identification code (SNID; Blondin & Tonry 2007). Several SNe Ic-BL that were not associated with GRBs, such as SN 1997ef (Iwamoto et al. 2000) and SN 2007I (Blondin et al. 2007), also provide good matches to SN 2013dx. In addition, D15 highlight similarities to the energetic SN 2010ah (PTF10bzf; Corsi et al. 2011; Mazzali et al. 2013).

5.3. *Photospheric Velocity Measurements*

In order to estimate the photospheric velocity of SN 2013dx, we measure the velocity of the most prominent spectral feature, the Si II 6355 Å absorption line. We employ a fitting code in `IDL` that removes the pseudo-continuum and fits a Gaussian to the absorption line (see Silverman et al. 2012 and Silverman et al. 2015 for a detailed description of the code). Table 3 displays the inferred velocities for each spectrum. Our results are also consistent with those reported by D15. The first three spectra ($\Delta t = 1.17$, 3.25, and 6.22 d) are too noisy for reliable velocity measurements.

5.4. *Line Identification*

We use SYN++ (Thomas et al. 2011) to help identify the ions present in our spectra of SN2013dx. SYN++ is derived from SYNOW (Fisher et al. 1997), which uses the Sobolev approximation (Sobolev 1960; Castor 1970; Jeffery 1989) to produce synthetic spectra of SNe during the photospheric phase. SYN++ assumes that spectral lines are formed via resonance scattering above a sharp photosphere. The location of the photosphere is expressed in velocity coordinates as $v_{\rm ph}$ (in $\rm km\,s^{-1}$) and takes into account the homologous expansion of the ejecta.

The optical depths for each species must also be input and line strengths are computed assuming Boltzmann excitation (i.e., local thermodynamic equilibrium) using a specified excitation temperature $T_{\rm exc}$ (in K). Non-local thermodynamic equilibrium effects are partially accounted for by allowing different $T_{\rm exc}$ values for each species, all of which can be different from the photospheric temperature $T_{\rm phot}$. The latter is used only in computing the blackbody radiation emitted by the photosphere.

We attempt to model the major spectral features of SN 2013dx at $\Delta t = 9.3$ and 33.3 d and looked for evolution during the photospheric phase (see Figure 9). At 9.3 d after the burst, SYN++ indicates a photospheric velocity of 30,000 $\rm km\,s^{-1}$, a maximum velocity of 90,000 $\rm km\,s^{-1}$, and a photospheric temperature of 16,000 K. The spectrum contains absorption from O I, Ca II, Si II, and Fe II, and possibly weak signatures of Fe III, Mg II, C II, and Na I. By 33.3 d after the burst, the SN ejecta have slowed down and cooled off significantly according to our second SYN++ fit. The photospheric velocity slows to 11,000 $\rm km\,s^{-1}$ with a maximum velocity of 60,000 $\rm km\,s^{-1}$ and photospheric temperature of 9000 K. The majority of the absorption in this spectrum is likely produced by Fe II and Ti II, though there are weak signatures of Si II, Ca II, and possibly O I as well. While the fit to this spectrum at wavelengths below $\sim$ 4700 Å is not perfect, the broad peaks and troughs roughly match. This part of the spectrum is notoriously difficult to model owing to hundreds of overlapping spectral features, mostly from iron-group elements.

6. SUPERNOVA EXPLOSION PARAMETERS

We model the basic explosion parameters of SN 2013dx by fitting its bolometric light curve with the Type I SN analytical model of Arnett (1982) and Valenti et al. (2008). This model assumes (1) homologous expansion of the ejecta, (2) spherical symmetry, (3) all ^{56}Ni is located at the center of explosion and no mixing, (4) radiation-

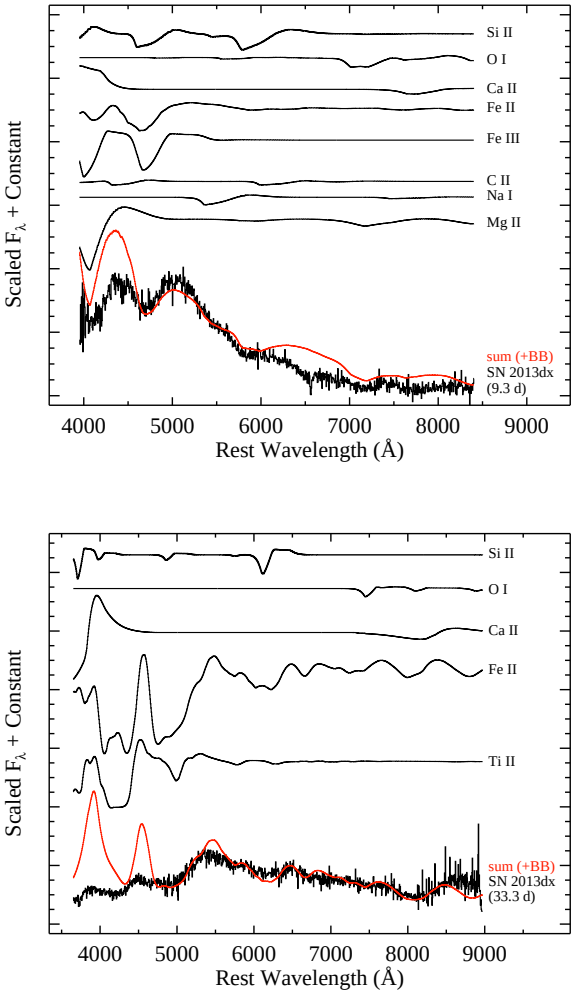

FIG. 9.— SYN++ fits to the 9.3 d (top) and 33.3 d (bottom) spectra of SN 2013dx. The spectrum of each individual ion is labeled. Their sum – plus a 16,000 K (top) and 9000 K (bottom) blackbody – is plotted in red on top of the actual observed spectra of SN 2013dx (binned to 6 Å per pixel).

pressure dominated ejecta, (5) the initial radius before explosion is small, (6) the diffusion approximation is appropriate for photons (i.e., the ejecta are in the photospheric phase), and (7) a single opacity over the duration of the explosion.

The peak luminosity correlates with the mass of ^{56}Ni, $M_{\rm Ni}$, while the light-curve shape is determined by the total ejecta mass, $M_{\rm ej}$, and the ejecta kinetic energy, $E_{\rm K}$. We can break the degeneracy between $M_{\rm ej}$ and $E_{\rm K}$ with photospheric velocity measurements from our optical spectra. Finally, we shall compare the derived explosion parameters for SN 2013dx with other GRB-associated SNe.

The timescale of the light curve is given by

$$\tau_m = \left(\frac{\kappa}{\beta c}\right)^{1/2}\left(\frac{6M_{\rm ej}^3}{5E_{\rm K}}\right)^{1/4}, \quad (3)$$

where $\beta \approx 13.8$ is an integration constant. For a uniform density (Arnett 1982) [25]

$$E_{\rm K} \approx \frac{3}{5}\frac{M_{\rm ej}v_{\rm ph}^2}{2}. \quad (4)$$

We assume $\kappa = 0.07\,{\rm cm^2\,g^{-1}}$ to directly compare with the literature for other GRB-SNe (e.g., Cano et al. 2011b).

We fit our quasi-bolometric light curve (§ 4.3) with the Arnett-Valenti relation,

$$L_{\rm ph}(t) = M_{\rm Ni}e^{-x^2} \times \left[(\epsilon_{\rm Ni}-\epsilon_{\rm Co})\int_0^x A(z)dz + \epsilon_{\rm Co}\int_0^x B(z)dz\right], \quad (5)$$

with

$$\begin{aligned} A(z) &= 2ze^{-2zy+z^2}, \\ B(z) &= 2ze^{-2zy+2zs+z^2}, \\ x &\equiv t/\tau_{\rm m}, \\ y &\equiv \tau_{\rm m}/(2\tau_{\rm Ni}), \text{ and} \\ s &\equiv \tau_m(\tau_{\rm Co}-\tau_{\rm Ni})/(2\tau_{\rm Co}\tau_{\rm Ni}). \end{aligned} \quad (6)$$

The decay times of ^{56}Ni and ^{56}Co are $\tau_{\rm Ni} = 8.77\,{\rm d}$ and $\tau_{\rm Co} = 111.3\,{\rm d}$, and the energies produced in one second by one gram of ^{56}Ni and ^{56}Co were taken as $\epsilon_{\rm Ni} = 3.90\times10^{10}\,{\rm erg\,s^{-1}\,g^{-1}}$ and $\epsilon_{\rm Co} = 6.78\times10^{9}\,{\rm erg\,s^{-1}\,g^{-1}}$ (Sutherland & Wheeler 1984; Cappellaro et al. 1997).

From our spectra and light curves, the SN component was dominant starting at $\Delta t \approx 4\,{\rm d}$ (compare with SN 2010bh, where shock breakout was prominent out to 7 d; Cano et al. 2011b). The Arnett-Valenti relation assumes that the material is in the photospheric phase, which is no longer valid at $\Delta t \gtrsim 30\,{\rm d}$. Therefore, our fit only includes $4 \le \Delta t \le 30\,{\rm d}$. We find $M_{\rm Ni} = 0.38\pm0.01\,{\rm M_\odot}$ and $\tau_{\rm m} = 11.32\pm0.17\,{\rm d}$ (statistical errors only). Using $v_{\rm ph} = 21,300{\rm km\,s^{-1}}$ from our spectral fit near peak (§ 5.3), we calculate $M_{\rm ej} = 3.0\pm0.1\,{\rm M_\odot}$ and $E_{\rm K} = (8.2\pm0.40)\times10^{51}\,{\rm erg}$. We note that opacity greatly affects $M_{\rm ej}$ and $E_{\rm K}$, and we report values for $\kappa = 0.01\ {\rm cm^2\ g^{-1}}$ ($M_{\rm ej} \approx 21\,rmM_\odot$, $E_{\rm K} \approx 6\times10^{52}\,{\rm erg}$) and $\kappa = 0.1\ {\rm cm^2\ g^{-1}}$ ($M_{\rm ej} \approx 2\,{\rm M_\odot}$, $E_{\rm K} \approx 6\times10^{51}\,{\rm erg}$). We also caution that numerical simulations of jet-driven SNe (e.g., González-Casanova et al. 2014; Mazzali et al. 2013; Umeda & Nomoto 2008) imply that the distribution of ^{56}Ni is likely to be highly asymmetric. The derived ejecta mass may therefore be biased by line-of-sight effects, and not representative of the total mass ejected in the explosion.

We compare our bolometric light curve of SN 2013dx with that of other spectroscopically confirmed GRB-SNe in Figure 7 (SN 1998bw, Galama et al. 1998; SN 2003lw, Mazzali et al. 2006; SN 2003dh, Deng et al. 2005; SN 2006aj, Pian et al. 2006; SN 2009nz, Olivares E. et al. 2015, SN 2010bh, Olivares E. et al. 2012b; SN 2011kl, Greiner et al. 2015; SN 2012bz: Melandri et al. 2012

[25] Note there is a typo incorrectly stating $E_{\rm K} \approx \frac{5}{3}\frac{M_{\rm ej}v_{\rm ph}^2}{2}$ in the original text that was corrected by Arnett (1996). This has been taken into accounted in Equations 3 and 4. This typo has been propagated throughout the literature.

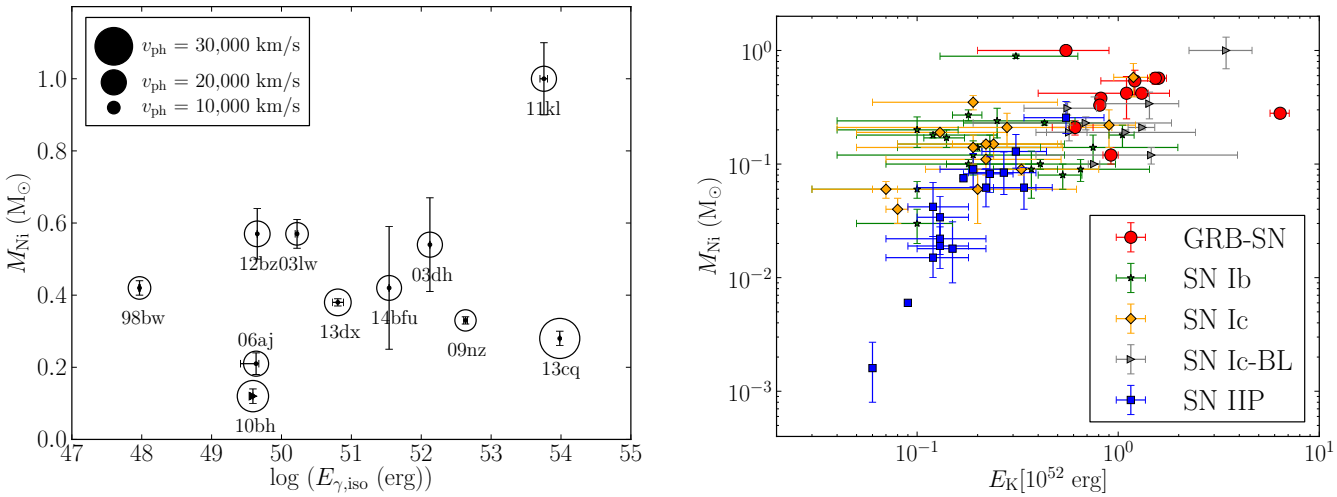

FIG. 10.— *(left)* Comparison of SN explosion parameters from template GRB-SNe and SN 2013dx from Table 4. The size of the points indicates v_{ph} near the SN brightness peak. There does not appear to be any correlation between M_{Ni} and $E_{\gamma,iso}$ or M_{Ni} and v_{ph}. *(right)* There is a clear correlation between explosion energy, E_k, and M_{Ni} for SNe Ib, Ic, Ic-BL (Cano 2013 and references therein), IIP (Hamuy 2003 and references therein), and GRB-SNe from Table 4. See Filippenko (1997) for a review of SN classification.

TABLE 4
PHYSICAL PARAMETERS OF GRB-SNE

GRB-SN	z	$E_{\gamma,iso}$ (erg)	v_{ph} (km s^{-1})	M_{Ni} ($M_\odot$)	M_{ej} ($M_\odot$)	E_k (10^{52} erg)	Reference
GRB 980425/SN 1998bw	0.0085	$(9.29 \pm 0.35) \times 10^{47}$	18,000	0.42 ± 0.02	6.80 ± 0.57	1.31 ± 0.10^a	(1), (2)
GRB 030329/SN 2003dh	0.1685	1.33×10^{52}	20,000	0.54 ± 0.13	5.06 ± 1.65	1.21 ± 0.39^a	(1), (2)
GRB 031203/SN 2003lw	0.105	$1.67^{+0.04}_{-0.10} \times 10^{50}$	18,000	0.57 ± 0.04	8.22 ± 0.76	1.59 ± 0.15^a	(1), (2)
GRB 060218/SN 2006aj	0.0335	$4.33^{+0.41}_{-1.74} \times 10^{49}$	20,000	0.21 ± 0.03	2.58 ± 0.55	0.61 ± 0.14^a	(1), (2)
GRB 091127/SN 2009nz	0.49	$(4.3 \pm 0.3) \times 10^{52}$	17,000	0.33 ± 0.01	4.69 ± 0.13	0.81 ± 0.02^a	(1), (3)
GRB 100316D/SN 2010bh[b]	0.059	$\geq (3.9 \pm 0.3) \times 10^{49}$	25,000	0.12 ± 0.02	2.47 ± 0.23	0.92 ± 0.08^a	(1), (4)
GRB 111209A/SN 2011kl[c]	0.677	$(5.7 \pm 0.7) \times 10^{53}$	20,000	1.0 ± 0.1	3.2 ± 0.5	0.55 ± 0.35	(5)
GRB 120422A/SN 2012bz[b]	0.283	4.5×10^{49}	20,500	0.57 ± 0.07	6.10 ± 0.49	1.53 ± 0.13^a	(1), (6)
GRB 130427A/SN 2013cq	0.3399	$(9.6 \pm 0.04) \times 10^{53}$	32,000	0.28 ± 0.02	6.27 ± 0.69	6.39 ± 0.70	(7)
GRB 130702A/SN 2013dx	0.145	$6.4^{+1.3}_{-1.0} \times 10^{50}$	21,300	0.38 ± 0.01	3.0 ± 0.1	0.82 ± 0.04	(8), (9)
GRB 140606B/iPTF14bfu	0.384	$(3.47 \pm 0.02) \times 10^{51}$	19,820	0.42 ± 0.17	4.8 ± 1.9	1.1 ± 0.7^a	(10)

NOTE. — [a] E_k originally calculated as $E_k = \frac{M_{ej} v_{ph}^2}{2}$, scaled by a factor of 3/5 to directly compare with our values. All $E_{\gamma,iso}$ values calculated over 1 keV – 10 MeV, except those indicated by superscript "b" which are calculated over 15–150 keV or superscript "c" which are calculated over 20–1400 keV. (1) Cano (2013), (2) Kaneko et al. (2007), (3) Troja et al. (2012), (4) Starling et al. (2011), (5) Greiner et al. (2015), (6) Zhang et al. (2012), (7) Xu et al. (2013), (8) Amati et al. (2013), (9) this work, (10) Cano et al. (2015).

and Schulze et al. 2014; SN 2013cq: Melandri et al. 2014; iPTF14bfu: Cano et al. 2015). We note that the NIR contribution to the bolometric luminosity for SN 2012bz is assumed to be the same as that observed for SN 2010bh. Although these GRB-SN bolometric light curves cover different wavelength ranges, we can get a sense of the light-curve evolution. SN 2013dx most closely matches the light-curve shape of SN 2012bz, but one caveat is that SN 2013dx has a steeper rise than SN 2012bz.

After 30 days, SN 2013dx appears to drop in luminosity rapidly. This is unlike the three bursts with late-time coverage – SN 2003lw, SN 2003dh, and SN 1998bw – seen particularly well juxtaposed against SN 1998bw, which has extensive observations out to hundreds of days. This drop in luminosity is not from underestimating the NIR contribution at late times; we still observe a rapid drop in luminosity at 30 d if we continue the monotonically increasing NIR ratio function from § 4.3 instead of adding a flat NIR contribution of 23% after 29 d.

In order to compare the derived properties of SN 2013dx with a broader sample of GRB-associated SNe, we use the derived values for M_{Ni}, M_{ej}, and E_K for all well-sampled events from Cano (2013). The authors fit a template of SN 1998bw to determine the appropriate stretch and scale parameters (e.g., § 4.2). Using average s and k values for each burst, the authors then fit a scaled version of the $UBVRIJH$ SN 1998bw light curve to the Arnett-Valenti model to derive the explosion parameters. This method has the benefit of (effectively) uniform wavelength coverage, even for events that were only observed in a few filters. However, the primary drawback is the assumption that all bolometric light curves are well-fit by an appropriately scaled version of SN 1998bw. As evidenced by Figure 6, this assumption breaks down at the very least for the redder filters for SN 2013dx (see also Lyman et al. 2014b). Nonetheless, the explosion parameters for all well-studied GRB-associated SNe derived in

this manner[26] are presented in Table 4.

In Figure 10 we plot the inferred $M_{\rm Ni}$ as a function of both the isotropic prompt gamma-ray energy release (left panel), as well as the derived SN kinetic energy ($E_{\rm K}$; right panel). It is clear that there is no correlation between $M_{\rm Ni}$ and the prompt energy release, as SN 2013dx has a comparable mass of synthesized ^{56}Ni as the subluminous GRB 980425 / SN 1998bw and the extremely luminous GRB 130427A / SN 2013cq (Levan et al. 2014; Melandri et al. 2014). Even if we were to apply a beaming correction, GRB 130427A would still have E_γ several orders of magnitude larger than GRB 980425 (Perley et al. 2014), but comparable $M_{\rm Ni}$. Similarly, there is no clear correlation between $M_{\rm Ni}$ and photospheric velocity at peak. Numerical simulations unambiguously predict that the mass of synthesized ^{56}Ni should be correlated with the degree of asymmetry in the explosion (González-Casanova et al. 2014; Umeda & Nomoto 2008); to the extent that our models faithfully reproduce the relevant (global) SN explosion parameters, this result is clearly not borne out by the data.

On the other hand, the explosion energy *of the SN ejecta* is clearly correlated with $M_{\rm Ni}$, particularly when including other core-collapse events. As shown by previous authors (e.g., Cano 2013 and Lyman et al. 2014b for recent compilations), GRB-associated SNe on average have a higher mass of synthesized ^{56}Ni and larger kinetic energies than any other class of core-collapse SNe (except perhaps the superluminous SNe; Gal-Yam 2012). That said, the SN explosion energies are typically narrowly clustered and do not appear to significantly exceed 10^{52} erg, consistent with (perhaps even indicative of) a magnetar origin for these events (Mazzali et al. 2014). SN 2013cq (associated with GRB 130427A) appears to be a significant outlier in terms of its inferred $E_{\rm K}$, however, which remains to be fully accounted for.

D15 created a bolometric light curve over the range 3000–10,000 Å extrapolated from u' and i'. We examined the bolometric light curve from D15 and found that our peak luminosity is consistent with theirs when accounting for our additional NIR coverage. D15 report $M_{\rm Ni} \approx 0.2\,{\rm M}_\odot$, a factor of two lower than our quoted value. On the other hand, they derive a total ejecta mass ($M_{\rm ej} \approx 7 \pm 2\,{\rm M}_\odot$) and a SN kinetic energy ($E_{\rm k} \approx (3.5 \pm 1.0) \times 10^{52}$ erg) approximately a factor of two larger than those presented here. D15 scale numerical simulations of the similarly shaped SN 2003dh (Mazzali et al. 2006) to estimate SN explosion parameters, as opposed to using an analytical model (e.g., Arnett-Valenti) used in this paper.

Since $M_{\rm Ni}$ is closely related to the peak luminosity, we believe our reported $M_{\rm Ni}$ estimate is more accurate than the value D15 report. When NIR contributions are included, SN 2013dx has a similar peak luminosity as SN 1998bw. We therefore expect SN 2013dx to have a similar ^{56}Ni mass as SN 1998bw. Both numerical simulations and analytical models produce $M_{\rm Ni} \approx 0.4\,{\rm M}_\odot$ for SN 1998bw (Mazzali et al. 2006; Cano 2013).

The discrepancy in ejecta mass and kinetic energy is caused mainly by different opacity assumptions. Mazzali et al. (2006) assumed an opacity, $\kappa = 0.5 Y_e\,{\rm cm^2\,g^{-1}}$, where Y_e is the number of electrons per baryon. We assume the authors used $Y_e = 0.46$ for iron and recalculate our Arnett-Valenti fit. With an opacity of $\kappa = 0.02\,{\rm cm^2\,g^{-1}}$, we report $M_{\rm ej} = 10.6 \pm 0.3\,{\rm M}_\odot$ and $E_{\rm k} = (2.9 \pm 0.2) \times 10^{52}$ erg. We also note that from our fit of SN 1998bw in §4.2, we can see that the light-curve evolution of SN 1998bw does not match that of SN 2013dx well (see Figure 6); hence, the different values of $M_{\rm ej}$ and $E_{\rm K}$ are not unexpected.

[26] We note that Cano (2013) and Cano et al. (2015) assume that $E_{\rm K} = \frac{M_{\rm ej} v_{\rm ph}^2}{2}$, so we scaled their reported $E_{\rm K}$ values by a factor of 3/5.

7. DISCUSSION/CONCLUSION

We present extensive optical and NIR photometry of GRB 130702A/SN 2013dx spanning 1–63 d after the gamma-ray trigger, and optical spectra covering 1–33 d after the trigger. At $z = 0.145$, GRB 130702A/SN 2013dx is sufficiently close to clearly detect and model the underlying SN component that emerged a week after the burst.

We isolate the SN component and present multi-band light curves, a quasi-bolometric ($g'r'i'z'yJ$) light curve, and spectra of SN 2013dx. Detection of the broad Si II λ6355 absorption line at velocities approaching $3 \times 10^4\,{\rm km\,s^{-1}}$, combined with the absence of H and He features, indicates that SN 2013dx is a broad-lined SN Ic. We estimate the SN explosion parameters using the Arnett-Valenti analytical relation and infer $M_{\rm Ni} = 0.38 \pm 0.01\,{\rm M}_\odot$, $M_{\rm ej} = 3.0 \pm 0.1\,{\rm M}_\odot$, and $E_{\rm K} = (8.2 \pm 0.4) \times 10^{51}$ erg.

Our analysis allows us to compare SN 2013dx with other GRB-SNe, as well as other core-collapse SNe (those of identical spectral type and not). This is of particular interest because GRB 130702A is of intermediate $E_{\gamma,{\rm iso}}$, between low-luminosity and cosmological GRBs. There seems to be no clear relation between $M_{\rm Ni}$, $M_{\rm ej}$, or $E_{\rm K}$ with GRB isotropic energy (Figure 10), even when considering beaming corrections. The SN appears to not be imprinted with any information about the formation of the relativistic jet aside from the high photospheric velocity and lack of H and He that allows us to classify all GRB-SNe as Type Ic-BL. This is somewhat puzzling, given the predictions of a correlation between the degree of asymmetry and mass of synthesized ^{56}Ni for jet-driven explosions. On the other hand, our observations do provide support for predictions that $M_{\rm Ni}$ should be strongly correlated with the kinetic energy of the SN itself.

Spectroscopically SN 2013dx resembles both other GRB-SNe like SN 2006aj and SN 1998bw, as well as non-GRB SN Ic-BL such as SN 1997ef, SN 2007I, and SN 2010ah. In terms of light curves, SN 2013dx most closely matches the evolution of SN 2012bz, associated with an intermediate GRB, but has a similar peak luminosity as SN 1998bw, associated with a low-luminosity GRB. Direct comparison of the light-curve evolution between SN 2013dx and SN 1998bw indicated that SN 2013dx has a quicker rise time than SN 1998bw. The faster rise time may indicate that SN 2013dx has a steeper distribution of ^{56}Ni in the outer layers of the star (i.e., less mixing) than SN 1998bw (Piro & Nakar 2013, Dessart et al. 2012).

Finally, we suggest two potential avenues for future study, especially with respect to GRB 130702A / SN 2013dx. Detailed numerical modeling of the SN ejecta

(e.g., Mazzali et al. 2006 for SN 1998bw), specifically tailored to the light curves and spectra of SN 2013dx (instead of simply scaling results from previous simulations), should help to improve the accuracy of estimates of the fundamental SN explosions parameters. In addition, a broadband study of the afterglow emission, in particular incorporating the radio emission, would enable a much improved estimate of the properties of the fastest-moving ejecta. This would greatly assist in placing GRB 130702A in the context of other relativistic explosions, specifically how the explosion energy is partitioned with respect to ejecta velocity (e.g., Margutti et al. 2014).

ACKNOWLEDGEMENTS

We gratefully acknowledge S. Schulze, F. Olivares, A. Melandri, and E. Pian for generously sharing their raw data, which significantly improved the analysis for this paper. We also thank J. Lyman for useful feedback on the manuscript.

This work was supported by the National Aeronautics and Space Administration (NASA) Headquarters under the NASA Earth and Space Science Fellowship Program (Grant NNX12AL70H) to V.T. The research of A.V.F.'s group at UC Berkeley has been funded by National Science Foundation (NSF) grant AST-1211916, Gary and Cynthia Bengier, the Richard and Rhoda Goldman Fund, the TABASGO Foundation, and the Christopher R. Redlich Fund. J.M.S. is supported by an NSF Astronomy and Astrophysics Postdoctoral Fellowship under award AST-1302771. A.G.Y. is supported by the EU/FP7 via ERC grant no. 307260, the Quantum Universe I-Core program by the Israeli Committee for planning and budgeting and the ISF; by Minerva and ISF grants; by the Weizmann-UK "making connections" program; and by Kimmel and ARCHES awards. A.C. acknowledges support from the NASA-*Swift* GI program via grants 13-SWIFT13-0030 and 14-SWIFT14-0024. E.T. acknowledges support for this project under the *Fermi* Guest Investigator Program. The work of D.S. was carried out at the Jet Propulsion Laboratory, California Institute of Technology, under a contract with NASA. We also acknowledge the help of K. Markey, E. Alduena, A. Alduena, and S. Kuo from Walden School for their help with the Palomar observations on 2013 July 8.

We thank the RATIR project team and the staff of the Observatorio Astronómico Nacional on Sierra San Pedro Mártir. RATIR is a collaboration between the University of California, the Universidad Nacional Autonóma de México, NASA Goddard Space Flight Center, and Arizona State University, benefiting from the loan of an H2RG detector and hardware and software support from Teledyne Scientific and Imaging. RATIR, the automation of the Harold L. Johnson Telescope of the Observatorio Astronómico Nacional on Sierra San Pedro Mártir, and the operation of both are funded through NASA grants NNX09AH71G, NNX09AT02G, NNX10AI27G, and NNX12AE66G, CONACyT grants INFR-2009-01-122785 and CB-2008-101958 , UNAM PAPIIT grant IN113810, and UC MEXUS-CONACyT grant CN 09-283.

These results made use of Lowell Observatory's Discovery Channel Telescope. Lowell operates the DCT in partnership with Boston University, Northern Arizona University, the University of Maryland, and the University of Toledo. Partial support of the DCT was provided by Discovery Communications. LMI was built by Lowell Observatory using funds from the National Science Foundation (AST-1005313). The Liverpool Telescope is operated on the island of La Palma by Liverpool John Moores University in the Spanish Observatorio del Roque de los Muchachos of the Instituto de Astrofisica de Canarias with financial support from the UK Science and Technology Facilities Council. Some of the data presented herein were obtained at the W. M. Keck Observatory, which is operated as a scientific partnership among the California Institute of Technology, the University of California, and NASA; the observatory was made possible by the generous financial support of the W. M. Keck Foundation.

This research has made use of the VizieR catalogue access tool, CDS, Strasbourg, France. This publication also uses data products from the Two Micron All Sky Survey, which is a joint project of the University of Massachusetts and the Infrared Processing and Analysis Center/California Institute of Technology, funded by NASA and the NSF. Funding for SDSS-III has been provided by the Alfred P. Sloan Foundation, the Participating Institutions, the NSF, and the U.S. Department of Energy Office of Science. The SDSS-III website is http://www.sdss3.org/. SDSS-III is managed by the Astrophysical Research Consortium for the Participating Institutions of the SDSS-III Collaboration including the University of Arizona, the Brazilian Participation Group, Brookhaven National Laboratory, Carnegie Mellon University, University of Florida, the French Participation Group, the German Participation Group, Harvard University, the Instituto de Astrofisica de Canarias, the Michigan State/Notre Dame/JINA Participation Group, Johns Hopkins University, Lawrence Berkeley National Laboratory, Max Planck Institute for Astrophysics, Max Planck Institute for Extraterrestrial Physics, New Mexico State University, New York University, Ohio State University, Pennsylvania State University, University of Portsmouth, Princeton University, the Spanish Participation Group, University of Tokyo, University of Utah, Vanderbilt University, University of Virginia, University of Washington, and Yale University.

REFERENCES

Aihara, H., Allende Prieto, C., An, D., et al. 2011, ApJS, 193, 29
Amati, L., Dichiara, S., Frontera, F., et al. 2013, GRB Coordinates Network, 15025, 1
Arnett, D. 1996, Supernovae and Nucleosynthesis: An Investigation of the History of Matter from the Big Bang to the Present (Princeton: Princeton University Press.)
Arnett, W. D. 1982, ApJ, 253, 785
Atwood, W. B., Abdo, A. A., Ackermann, M., et al. 2009, ApJ, 697, 1071
Bennett, C. L., Larson, D., Weiland, J. L., & Hinshaw, G. 2014, ApJ, 794, 135
Berger, E., Kulkarni, S. R., Frail, D. A., & Soderberg, A. M. 2003, ApJ, 599, 408
Berger, E., Chornock, R., Holmes, T. R., et al. 2011, ApJ, 743, 204

Bertin, E. 2006, in Astronomical Society of the Pacific Conference Series, Vol. 351, Astronomical Data Analysis Software and Systems XV, ed. C. Gabriel, C. Arviset, D. Ponz, & S. Enrique, 112
Bertin, E., & Arnouts, S. 1996, A&AS, 117, 393
Bertin, E., Mellier, Y., Radovich, M., et al. 2002, in Astronomical Society of the Pacific Conference Series, Vol. 281, Astronomical Data Analysis Software and Systems XI, ed. D. A. Bohlender, D. Durand, & T. H. Handley, 228
Bietenholz, M. F., De Colle, F., Granot, J., Bartel, N., & Soderberg, A. M. 2014, MNRAS, 440, 821
Blanton, M. R., & Roweis, S. 2007, AJ, 133, 734
Blondin, S., Modjaz, M., Kirshner, R., Challis, P., & Calkins, M. 2007, Central Bureau Electronic Telegrams, 808, 1
Blondin, S., & Tonry, J. L. 2007, ApJ, 666, 1024
Bromberg, O., Nakar, E., & Piran, T. 2011, ApJ, 739, L55
Bufano, F., Pian, E., Sollerman, J., et al. 2012, ApJ, 753, 67
Burrows, D. N., Hill, J. E., Nousek, J. A., et al. 2005, Space Sci. Rev., 120, 165
Butler, N., Klein, C., Fox, O., et al. 2012, in Society of Photo-Optical Instrumentation Engineers (SPIE) Conference Series, Vol. 8446, 10
Butler, N., Watson, A. M., Kutyrev, A., et al. 2013, GRB Coordinates Network, 14993, 1
Campana, S., Mangano, V., Blustin, A. J., et al. 2006, Nature, 442, 1008
Cano, Z. 2013, MNRAS, 434, 1098
—. 2014, ApJ, 794, 121
Cano, Z., Bersier, D., Guidorzi, C., et al. 2011a, ApJ, 740, 41
—. 2011b, ApJ, 740, 41
Cano, Z., de Ugarte Postigo, A., Perley, D., et al. 2015, arXiv e-prints (astro-ph/1505.03522), arXiv:1505.03522
Cappellaro, E., Mazzali, P. A., Benetti, S., et al. 1997, A&A, 328, 203
Cardelli, J. A., Clayton, G. C., & Mathis, J. S. 1989, ApJ, 345, 245
Castor, J. I. 1970, MNRAS, 149, 111
Cenko, S. B., Gal-Yam, A., Kasliwal, M. M., et al. 2013, GRB Coordinates Network, 14998, 1
Cenko, S. B., Fox, D. B., Moon, D.-S., et al. 2006, PASP, 118, 1396
Cenko, S. B., Fox, D. B., Penprase, B. E., et al. 2008, ApJ, 677, 441
Cheung, T., Vianello, G., Zhu, S., et al. 2013, GRB Coordinates Network, 14971, 1
Chornock, R., Berger, E., Levesque, E. M., et al. 2010, ArXiv e-prints, arXiv:1004.2262
Clocchiatti, A., Suntzeff, N. B., Covarrubias, R., & Candia, P. 2011, AJ, 141, 163
Cobb, B. E., Bloom, J. S., Perley, D. A., et al. 2010, ApJ, 718, L150
Collazzi, A. C., & Connaughton, V. 2013, GRB Coordinates Network, 14972, 1
Corsi, A., Ofek, E. O., Frail, D. A., et al. 2011, ApJ, 741, 76
Covino, S., Melandri, A., Salvaterra, R., et al. 2013, MNRAS, 432, 1231
D'Avanzo, P., D'Elia, V., Tagliaferri, G., et al. 2013, GRB Coordinates Network, 14984, 1
D'Elia, V., D'Avanzo, P., Melandri, A., et al. 2013, GRB Coordinates Network, 15000, 1
D'Elia, V., Pian, E., Melandri, A., et al. 2015, A&A, 577, A116
Della Valle, M., Chincarini, G., Panagia, N., et al. 2006, Nature, 444, 1050
Deng, J., Tominaga, N., Mazzali, P. A., Maeda, K., & Nomoto, K. 2005, ApJ, 624, 898
Dessart, L., Hillier, D. J., Li, C., & Woosley, S. 2012, MNRAS, 424, 2139
Drout, M. R., Soderberg, A. M., Gal-Yam, A., et al. 2011, ApJ, 741, 97
Evans, P. A., Beardmore, A. P., Page, K. L., et al. 2009, MNRAS, 397, 1177
Faber, S. M., Phillips, A. C., Kibrick, R. I., et al. 2003, in Society of Photo-Optical Instrumentation Engineers (SPIE) Conference Series, Vol. 4841, Instrument Design and Performance for Optical/Infrared Ground-based Telescopes, ed. M. Iye & A. F. M. Moorwood, 1657–1669
Ferrero, P., Kann, D. A., Zeh, A., et al. 2006, A&A, 457, 857
Filippenko, A. V. 1982, PASP, 94, 715
—. 1997, ARA&A, 35, 309
Fisher, A., Branch, D., Nugent, P., & Baron, E. 1997, ApJ, 481, L89
Fox, O. D., Kutyrev, A. S., Rapchun, D. A., et al. 2012, in Society of Photo-Optical Instrumentation Engineers (SPIE) Conference Series, Vol. 8453, 1
Fynbo, J. P. U., Watson, D., Thöne, C. C., et al. 2006, Nature, 444, 1047
Gal-Yam, A. 2012, Science, 337, 927
Gal-Yam, A., Moon, D.-S., Fox, D. B., et al. 2004, ApJ, 609, L59
Gal-Yam, A., Fox, D. B., Price, P. A., et al. 2006, Nature, 444, 1053
Galama, T. J., Vreeswijk, P. M., van Paradijs, J., et al. 1998, Nature, 395, 670
Gehrels, N., Chincarini, G., Giommi, P., et al. 2004, ApJ, 611, 1005
Golenetskii, S., Aptekar, R., Pal'Shin, V., et al. 2013, GRB Coordinates Network, 14986, 1
González-Casanova, D. F., De Colle, F., Ramirez-Ruiz, E., & Lopez, L. A. 2014, ApJ, 781, L26
Graham, J. F., & Fruchter, A. S. 2013, ApJ, 774, 119
Greiner, J., Mazzali, P. A., Kann, D. A., et al. 2015, Nature, 523, 189
Hamuy, M. 2003, ApJ, 582, 905
Hjorth, J., & Bloom, J. S. 2012, The Gamma-Ray Burst - Supernova Connection (Cambridge University Press: Cambridge), 169–190
Hogg, D. W., Baldry, I. K., Blanton, M. R., & Eisenstein, D. J. 2002, arXiV e-prints (astro-ph/0210394), astro-ph/0210394
Horne, K. 1986, PASP, 98, 609
Iwamoto, K., Mazzali, P. A., Nomoto, K., et al. 1998, Nature, 395, 672
Iwamoto, K., Nakamura, T., Nomoto, K., et al. 2000, ApJ, 534, 660
Jeffery, D. J. 1989, ApJS, 71, 951
Kalberla, P. M. W., Burton, W. B., Hartmann, D., et al. 2005, A&A, 440, 775
Kaneko, Y., Ramirez-Ruiz, E., Granot, J., et al. 2007, ApJ, 654, 385
Kelly, P. L., Filippenko, A. V., Fox, O. D., Zheng, W., & Clubb, K. I. 2013, ApJ, 775, L5
Kelson, D. D. 2003, PASP, 115, 688
Kinney, A. L., Calzetti, D., Bohlin, R. C., et al. 1996, ApJ, 467, 38
Kocevski, D., Modjaz, M., Bloom, J. S., et al. 2007, ApJ, 663, 1180
Kulkarni, S. R., Frail, D. A., Wieringa, M. H., et al. 1998, Nature, 395, 663
Lang, D., Hogg, D. W., Mierle, K., Blanton, M., & Roweis, S. 2010, AJ, 139, 1782
Law, N. M., Kulkarni, S. R., Dekany, R. G., et al. 2009, PASP, 121, 1395
Levan, A. J., Tanvir, N. R., Fruchter, A. S., et al. 2014, ApJ, 792, 115
Lyman, J., Bersier, D., James, P., et al. 2014a, ArXiv e-prints, arXiv:1406.3667
—. 2014b, ArXiv e-prints, arXiv:1406.3667
Lyman, J. D., Bersier, D., & James, P. A. 2014c, MNRAS, 437, 3848
Malesani, D., Tagliaferri, G., Chincarini, G., et al. 2004, ApJ, 609, L5
Margutti, R., Milisavljevic, D., Soderberg, A. M., et al. 2014, ApJ, 797, 107
Matheson, T., Filippenko, A. V., Ho, L. C., Barth, A. J., & Leonard, D. C. 2000, AJ, 120, 1499
Matheson, T., Garnavich, P. M., Stanek, K. Z., et al. 2003, ApJ, 599, 394
Mazzali, P. A., McFadyen, A. I., Woosley, S. E., Pian, E., & Tanaka, M. 2014, MNRAS, 443, 67
Mazzali, P. A., Walker, E. S., Pian, E., et al. 2013, MNRAS, 432, 2463
Mazzali, P. A., Deng, J., Pian, E., et al. 2006, ApJ, 645, 1323
McLean, I. S., Steidel, C. C., Epps, H. W., et al. 2012, in Society of Photo-Optical Instrumentation Engineers (SPIE) Conference Series, Vol. 8446, 0
Meegan, C., Lichti, G., Bhat, P. N., et al. 2009, ApJ, 702, 791

Melandri, A., Pian, E., Ferrero, P., et al. 2012, A&A, 547, A82
Melandri, A., Pian, E., D'Elia, V., et al. 2014, A&A, 567, A29
Mirabal, N., Halpern, J. P., An, D., Thorstensen, J. R., & Terndrup, D. M. 2006, ApJ, 643, L99
Modjaz, M., Stanek, K. Z., Garnavich, P. M., et al. 2006a, ApJ, 645, L21
—. 2006b, ApJ, 645, L21
Modjaz, M., Kewley, L., Kirshner, R. P., et al. 2008, AJ, 135, 1136
Modjaz, M., Li, W., Butler, N., et al. 2009, ApJ, 702, 226
Mulchaey, J., Kasliwal, M. M., Arcavi, I., Bellm, E., & Kelson, D. 2013a, GRB Coordinates Network, 14985, 1
—. 2013b, The Astronomer's Telegram, 5191, 1
Nakar, E. 2015, arXiv e-prints (astro-ph/1503.00441), arXiv:1503.00441
Oke, J. B., & Gunn, J. E. 1982, PASP, 94, 586
—. 1983, ApJ, 266, 713
Oke, J. B., Cohen, J. G., Carr, M., et al. 1995, PASP, 107, 375
Olivares E., F., Greiner, J., Schady, P., et al. 2012a, A&A, 539, A76
—. 2012b, A&A, 539, A76
—. 2015, A&A, 577, A44
Patat, F., Cappellaro, E., Danziger, J., et al. 2001, ApJ, 555, 900
Pei, Y. C. 1992, ApJ, 395, 130
Perley, D. A., Cenko, S. B., Corsi, A., et al. 2014, ApJ, 781, 37
Phillips, M. M. 1993, ApJ, 413, L105
Pian, E., Mazzali, P. A., Masetti, N., et al. 2006, Nature, 442, 1011
Piro, A. L., & Nakar, E. 2013, ApJ, 769, 67
Racusin, J. L., Liang, E. W., Burrows, D. N., et al. 2009, ApJ, 698, 43
Rau, A., Kulkarni, S. R., Law, N. M., et al. 2009, PASP, 121, 1334
Sari, R., Piran, T., & Narayan, R. 1998, ApJ, 497, L17
Schlafly, E. F., & Finkbeiner, D. P. 2011, ApJ, 737, 103
Schulze, S., Leloudas, G., Xu, D., et al. 2013, GRB Coordinates Network, 14994, 1
Schulze, S., Malesani, D., Cucchiara, A., et al. 2014, A&A, 566, A102
Silverman, J. M., Kong, J. J., & Filippenko, A. V. 2012, MNRAS, 425, 1819
Silverman, J. M., Vinko, J., Marion, G. H., et al. 2015, MNRAS, 451, 1973
Singer, L. P., Cenko, S. B., Kasliwal, M. M., et al. 2013a, ApJ, 776, L34
—. 2013b, GRB Coordinates Network, 14967, 1
Skrutskie, M. F., Cutri, R. M., Stiening, R., et al. 2006, AJ, 131, 1163
Sobolev, V. V. 1960, Moving envelopes of stars (Cambridge: Harvard University Press)
Soderberg, A. M., Chakraborti, S., Pignata, G., et al. 2010, Nature, 463, 513
Sollerman, J., Holland, S. T., Challis, P., et al. 2002, A&A, 386, 944
Sollerman, J., Jaunsen, A. O., Fynbo, J. P. U., et al. 2006, A&A, 454, 503
Stanek, K. Z., Matheson, T., Garnavich, P. M., et al. 2003, ApJ, 591, L17
Starling, R. L. C., Wiersema, K., Levan, A. J., et al. 2011, MNRAS, 411, 2792
Steele, I. A., Smith, R. J., Rees, P. C., et al. 2004, in Society of Photo-Optical Instrumentation Engineers (SPIE) Conference Series, Vol. 5489, Ground-based Telescopes, ed. J. M. Oschmann, Jr., 679–692
Sutherland, P. G., & Wheeler, J. C. 1984, ApJ, 280, 282
Thomas, R. C., Nugent, P. E., & Meza, J. C. 2011, PASP, 123, 237
Thomsen, B., Hjorth, J., Watson, D., et al. 2004, A&A, 419, L21
Troja, E., Sakamoto, T., Guidorzi, C., et al. 2012, ApJ, 761, 50
Umeda, H., & Nomoto, K. 2008, ApJ, 673, 1014
Valenti, S., Benetti, S., Cappellaro, E., et al. 2008, MNRAS, 383, 1485
Wade, R. A., & Horne, K. 1988, ApJ, 324, 411
Watson, A. M., Richer, M. G., Bloom, J. S., et al. 2012, in Society of Photo-Optical Instrumentation Engineers (SPIE) Conference Series, Vol. 8444, 5
Woosley, S. E., & Bloom, J. S. 2006, ARA&A, 44, 507
Xu, D., de Ugarte Postigo, A., Leloudas, G., et al. 2013, ApJ, 776, 98
Yaron, O., & Gal-Yam, A. 2012, PASP, 124, 668
Zhang, B.-B., Fan, Y.-Z., Shen, R.-F., et al. 2012, ApJ, 756, 190

TABLE 5
Imaging log

Filter	Epoch (days)	Telescope	Exp. (s)	AB mag
u'	330.49	Keck/LRIS	203	24.50 ± 0.14
g'	1.17	P60	120	18.80 ± 0.04
g'	1.26	P60	120	18.86 ± 0.04
g'	2.21	P60	270	19.52 ± 0.04
g'	3.23	P60	450	20.02 ± 0.05
g'	4.19	P60	1260	20.22 ± 0.04
g'	5.27	P60	540	20.35 ± 0.04
g'	6.28	P60	540	20.31 ± 0.04
g'	7.20	P60	720	20.32 ± 0.04
g'	9.87	Liverpool	130	20.35 ± 0.33
g'	10.87	Liverpool	130	20.39 ± 0.35
g'	11.26	P60	720	20.22 ± 0.05
g'	11.87	Liverpool	130	20.06 ± 0.21
g'	12.18	P60	660	20.23 ± 0.03
g'	12.86	Liverpool	130	20.00 ± 0.23
g'	13.86	Liverpool	130	20.39 ± 0.34
g'	14.18	P60	720	20.31 ± 0.06
g'	15.18	P60	720	20.43 ± 0.07
g'	16.18	P60	720	20.36 ± 0.13
g'	17.87	Liverpool	150	20.32 ± 0.13
g'	19.87	Liverpool	150	20.78 ± 0.19
g'	21.87	Liverpool	150	20.98 ± 0.15
g'	23.87	Liverpool	150	21.25 ± 0.30
g'	27.92	Liverpool	150	21.53 ± 0.07
g'	29.21	P60	540	21.62 ± 0.12
g'	30.19	P60	1080	21.72 ± 0.09
g'	34.17	P60	1080	21.84 ± 0.08
g'	37.89	Liverpool	450	22.06 ± 0.08
g'	39.88	Liverpool	450	22.11 ± 0.09
g'	45.88	Liverpool	450	22.64 ± 0.34
g'	53.88	Liverpool	150	22.42 ± 0.07
g'	58.88	Liverpool	150	22.56 ± 0.06
g'	62.87	Liverpool	150	22.60 ± 0.09
g'	330.48	Keck/LRIS	203	23.51 ± 0.03
g'	632.37	DCT	1200	23.66 ± 0.04
r'	0.18	P48	60	17.38 ± 0.04
r'	0.21	P48	60	17.52 ± 0.04
r'	1.26	P60	360	18.66 ± 0.05
r'	2.16	RATIR	7600	19.23 ± 0.06
r'	2.21	P60	420	19.32 ± 0.04
r'	3.21	RATIR	5040	19.67 ± 0.04
r'	3.25	P60	120	19.70 ± 0.08
r'	4.18	P60	1320	19.97 ± 0.04
r'	4.21	RATIR	5360	19.88 ± 0.05
r'	5.21	RATIR	4960	19.95 ± 0.05
r'	5.27	P60	540	20.00 ± 0.04
r'	6.20	RATIR	4880	19.94 ± 0.05
r'	6.27	P60	540	20.04 ± 0.04
r'	7.19	RATIR	2640	19.90 ± 0.05
r'	7.19	P60	720	20.06 ± 0.04
r'	8.22	RATIR	3920	19.82 ± 0.05
r'	9.87	Liverpool	130	19.86 ± 0.07
r'	10.87	Liverpool	130	19.69 ± 0.07
r'	11.25	P60	660	19.82 ± 0.02
r'	11.87	Liverpool	130	19.73 ± 0.07
r'	12.18	P60	660	19.78 ± 0.04
r'	12.22	RATIR	2880	19.70 ± 0.04
r'	12.87	Liverpool	130	19.74 ± 0.08
r'	13.16	RATIR	1280	19.68 ± 0.05
r'	13.87	Liverpool	130	19.68 ± 0.10
r'	14.18	P60	660	19.70 ± 0.04
r'	14.18	RATIR	3760	19.68 ± 0.07
r'	15.16	RATIR	5280	19.70 ± 0.05
r'	15.17	P60	660	19.64 ± 0.04
r'	15.87	Liverpool	150	19.80 ± 0.07
r'	16.17	P60	660	19.76 ± 0.08
r'	17.87	Liverpool	150	19.83 ± 0.03
r'	19.87	Liverpool	150	19.92 ± 0.04
r'	21.88	Liverpool	150	20.00 ± 0.03
r'	23.87	Liverpool	150	20.20 ± 0.02
r'	25.17	RATIR	4560	20.16 ± 0.07
r'	26.15	RATIR	2160	20.22 ± 0.05

TABLE 5 — *Continued*

Filter	Epoch (days)	Telescope	Exp. (s)	AB mag
r'	27.15	RATIR	5200	20.31 ± 0.05
r'	27.91	Liverpool	150	20.42 ± 0.03
r'	28.16	RATIR	5120	20.38 ± 0.05
r'	29.15	RATIR	5200	20.52 ± 0.06
r'	29.19	P60	540	20.49 ± 0.05
r'	30.18	P60	540	20.54 ± 0.06
r'	30.19	RATIR	3120	20.63 ± 0.06
r'	31.15	RATIR	3920	20.62 ± 0.15
r'	32.15	RATIR	4960	20.73 ± 0.06
r'	34.16	P60	540	20.87 ± 0.07
r'	35.17	RATIR	3680	20.96 ± 0.06
r'	37.88	Liverpool	150	21.22 ± 0.04
r'	39.88	Liverpool	150	21.27 ± 0.06
r'	41.16	RATIR	3840	21.25 ± 0.08
r'	45.15	RATIR	2080	21.33 ± 0.12
r'	45.87	Liverpool	150	21.46 ± 0.14
r'	46.15	RATIR	3120	21.36 ± 0.11
r'	47.88	Liverpool	150	21.42 ± 0.15
r'	53.87	Liverpool	150	21.75 ± 0.06
r'	58.87	Liverpool	150	21.81 ± 0.06
r'	62.86	Liverpool	150	21.80 ± 0.10
R	330.48	Keck/LRIS	200	23.26 ± 0.06
r'	632.39	DCT	1200	23.15 ± 0.04
i'	1.17	P60	120	18.42 ± 0.04
i'	1.26	P60	120	18.56 ± 0.06
i'	2.16	RATIR	7600	19.09 ± 0.07
i'	2.21	P60	420	19.12 ± 0.04
i'	3.21	RATIR	5040	19.59 ± 0.06
i'	3.24	P60	450	19.64 ± 0.05
i'	4.17	P60	1320	19.97 ± 0.06
i'	4.21	RATIR	5360	19.93 ± 0.06
i'	5.21	RATIR	4960	20.05 ± 0.12
i'	5.26	P60	540	20.13 ± 0.05
i'	6.20	RATIR	4880	20.13 ± 0.09
i'	6.27	P60	660	20.09 ± 0.05
i'	7.18	P60	660	20.17 ± 0.05
i'	7.19	RATIR	3280	20.07 ± 0.17
i'	8.22	RATIR	3920	20.10 ± 0.07
i'	9.87	Liverpool	130	19.93 ± 0.13
i'	10.87	Liverpool	130	19.86 ± 0.16
i'	11.17	P60	180	19.88 ± 0.11
i'	11.87	Liverpool	130	19.87 ± 0.15
i'	12.19	P60	660	19.94 ± 0.04
i'	12.22	RATIR	2880	19.91 ± 0.05
i'	12.87	Liverpool	130	19.94 ± 0.14
i'	13.16	RATIR	1280	19.86 ± 0.05
i'	13.87	Liverpool	130	20.01 ± 0.21
i'	14.18	RATIR	3760	19.84 ± 0.05
i'	14.19	P60	660	19.86 ± 0.06
i'	15.16	RATIR	5280	19.83 ± 0.05
i'	15.19	P60	660	19.77 ± 0.06
i'	15.87	Liverpool	150	19.91 ± 0.10
i'	16.19	P60	660	20.02 ± 0.10
i'	17.87	Liverpool	150	19.94 ± 0.07
i'	19.87	Liverpool	150	19.88 ± 0.05
i'	21.87	Liverpool	150	19.97 ± 0.04
i'	23.87	Liverpool	150	20.09 ± 0.05
i'	25.17	RATIR	4560	20.04 ± 0.06
i'	26.15	RATIR	2160	20.09 ± 0.05
i'	27.15	RATIR	5200	20.15 ± 0.06
i'	27.91	Liverpool	150	20.18 ± 0.02
i'	28.16	RATIR	5120	20.21 ± 0.05
i'	29.15	RATIR	5200	20.30 ± 0.07
i'	29.22	P60	540	20.31 ± 0.06
i'	30.19	RATIR	3120	20.41 ± 0.07
i'	30.20	P60	540	20.44 ± 0.08
i'	31.15	RATIR	4000	20.43 ± 0.14
i'	32.15	RATIR	5440	20.52 ± 0.07
i'	34.18	P60	540	20.67 ± 0.07
i'	35.17	RATIR	3680	20.68 ± 0.07
i'	37.88	Liverpool	150	21.01 ± 0.05
i'	39.87	Liverpool	150	21.03 ± 0.08
i'	41.16	RATIR	3840	20.88 ± 0.08

TABLE 5 — *Continued*

Filter	Epoch (days)	Telescope	Exp. (s)	AB mag
i'	45.15	RATIR	2080	21.05 ± 0.11
i'	45.87	Liverpool	150	21.16 ± 0.10
i'	46.15	RATIR	3120	21.12 ± 0.10
i'	47.88	Liverpool	150	21.14 ± 0.13
i'	53.86	Liverpool	150	21.56 ± 0.09
i'	58.86	Liverpool	150	21.65 ± 0.09
i'	62.86	Liverpool	150	21.53 ± 0.12
i'	632.39	DCT	1200	23.03 ± 0.06
z'	2.16	RATIR	5700	18.91 ± 0.09
z'	2.21	P60	870	19.02 ± 0.08
z'	3.21	RATIR	3780	19.36 ± 0.07
z'	3.24	P60	840	19.43 ± 0.09
z'	4.19	P60	1320	19.53 ± 0.10
z'	4.21	RATIR	4020	19.72 ± 0.12
z'	5.20	P60	1020	19.84 ± 0.12
z'	5.21	RATIR	3720	19.84 ± 0.08
z'	6.20	RATIR	3660	19.94 ± 0.11
z'	6.26	P60	540	19.95 ± 0.12
z'	7.18	P60	540	20.04 ± 0.11
z'	7.19	RATIR	2820	19.71 ± 0.35
z'	8.22	RATIR	2940	19.98 ± 0.13
z'	9.87	Liverpool	150	20.11 ± 0.12
z'	10.87	Liverpool	150	19.99 ± 0.12
z'	11.87	Liverpool	150	20.13 ± 0.11
z'	12.22	RATIR	2160	19.94 ± 0.13
z'	12.87	Liverpool	150	20.02 ± 0.11
z'	13.16	RATIR	960	20.02 ± 0.12
z'	13.87	Liverpool	150	19.82 ± 0.13
z'	14.18	RATIR	2820	19.87 ± 0.12
z'	15.16	RATIR	3960	20.01 ± 0.10
z'	15.87	Liverpool	150	20.21 ± 0.20
z'	17.88	Liverpool	150	20.10 ± 0.08
z'	19.88	Liverpool	150	20.08 ± 0.05
z'	21.88	Liverpool	150	20.19 ± 0.06
z'	23.88	Liverpool	150	20.27 ± 0.04
z'	25.17	RATIR	3300	20.46 ± 0.14
z'	26.15	RATIR	1560	20.06 ± 0.13
z'	27.15	RATIR	3900	20.30 ± 0.09
z'	27.90	Liverpool	150	20.33 ± 0.07
z'	28.16	RATIR	3780	20.23 ± 0.09
z'	29.15	RATIR	3900	20.49 ± 0.10
z'	30.19	RATIR	2340	20.44 ± 0.15
z'	31.15	RATIR	2940	20.45 ± 0.11
z'	32.15	RATIR	4080	20.81 ± 0.15
z'	34.15	RATIR	3660	20.87 ± 0.12
z'	35.17	RATIR	2820	20.96 ± 0.14
z'	37.87	Liverpool	150	21.15 ± 0.15
z'	39.87	Liverpool	150	21.33 ± 0.20
z'	45.86	Liverpool	150	21.41 ± 0.30
z'	53.85	Liverpool	150	21.27 ± 0.13
z'	58.85	Liverpool	150	21.60 ± 0.20
z'	62.85	Liverpool	150	21.85 ± 0.29
z'	632.41	DCT	1200	23.02 ± 0.12
y	2.16	RATIR	5700	18.78 ± 0.08
y	3.21	RATIR	3780	19.23 ± 0.08
y	4.21	RATIR	4020	19.53 ± 0.09
y	5.21	RATIR	3720	19.70 ± 0.09
y	6.20	RATIR	3660	19.79 ± 0.07
y	12.22	RATIR	2160	19.49 ± 0.10
y	13.16	RATIR	960	19.70 ± 0.13
y	14.18	RATIR	2820	19.75 ± 0.09
y	15.16	RATIR	3960	19.73 ± 0.11
y	22.16	RATIR	2340	19.85 ± 0.13
y	25.17	RATIR	3300	19.69 ± 0.14
y	26.15	RATIR	1560	20.00 ± 0.13
y	27.15	RATIR	3900	20.05 ± 0.09
y	28.16	RATIR	3780	20.01 ± 0.09
y	29.15	RATIR	3900	20.03 ± 0.10
y	30.19	RATIR	2340	20.04 ± 0.11
y	31.15	RATIR	2940	20.28 ± 0.12
y	32.15	RATIR	4080	20.00 ± 0.11
y	34.15	RATIR	3660	20.49 ± 0.14
y	35.17	RATIR	2820	20.51 ± 0.14
J	2.16	RATIR	6380	18.75 ± 0.09

TABLE 5 — *Continued*

Filter	Epoch (days)	Telescope	Exp. (s)	AB mag
J	3.21	RATIR	4230	19.22 ± 0.07
J	4.21	RATIR	4500	19.65 ± 0.09
J	5.21	RATIR	4160	19.64 ± 0.10
J	6.20	RATIR	4090	19.85 ± 0.10
J	14.18	RATIR	3150	20.07 ± 0.12
J	15.16	RATIR	4430	19.86 ± 0.11
J	27.15	RATIR	4360	19.92 ± 0.13
J	28.16	RATIR	4230	20.05 ± 0.12
J	29.15	RATIR	4360	20.23 ± 0.13
J	349.45	Keck/MOSFIRE	132	23.18 ± 0.32
H	2.16	RATIR	6380	18.60 ± 0.09
H	3.21	RATIR	4230	18.96 ± 0.08
H	4.21	RATIR	4500	19.37 ± 0.11
H	5.21	RATIR	4160	19.83 ± 0.12
H	6.20	RATIR	4090	19.89 ± 0.13
K_s	349.44	Keck/MOSFIRE	79	> 22.29

NOTE. — AB magnitudes, not corrected for Galactic extinction.